Journal of Materials Research and Technology 41 (2026) 7378–7398

Contents lists available at ScienceDirect

Journal of Materials Research and Technology

journal homepage: www.elsevier.com/locate/jmrt

Understanding failure in austenitic steels: Key considerations for molten salt storage in CSP applications☆

Sergio Andrés Ardila-Parra [a], Cristina Prieto [b], Julian D. Osorio [c], Ana I. Fernández [a,*]

[a] DIOPMA Research Group, Departament de Ciència de Materials I Química Física, Universitat de Barcelona, C/ Martí I Franquès 1, 08028, Barcelona, Spain
[b] Department of Energy Engineering, Universidad de Sevilla, 41092, Sevilla, Spain
[c] Building Technologies and Science Center, National Laboratory of the Rockies, Golden, CO, 80401, United States of America

A B S T R A C T

Owing to their excellent properties, austenitic stainless steels are extensively used in boilers, furnaces, molten salt tanks, and other applications that are subjected to extreme mechanical loads and high-temperature conditions. Their high corrosion and creep resistance make them suitable for high-temperature operating environments. Additionally, good fatigue resistance and favorable mechanical and visual properties are essential. However, the premature failure of several components at elevated temperatures has been previously reported. Although the failure analysis of components in service is complex, processes such as cold work and welding have been identified as contributing factors to the performance degradation of these steels. This study aims to analyze the various documented failure modes and mechanisms in austenitic steels, including creep, cracking, stress relaxation cracking, and fatigue, to better understand the multi-objective design requirements for these alloys as structural materials for high-temperature molten salt tanks in Concentrating Solar Power (CSP) plants. Stabilized austenitic grades, such as AISI 347H, demonstrate superior resistance to creep and corrosion-related degradation when compared to non-stabilized grades like AISI 316L at temperatures relevant to concentrated solar power (CSP) applications. In contrast, nickel-based alloys offer enhanced corrosion resistance, albeit at a higher cost. This review underscores that creep, stress relaxation cracking, and thermo-mechanical fatigue are the predominant long-term failure risks in CSP hot tanks.

1. Introduction

Concentrating Solar Power (CSP) is a commercially deployed technology that offers a promising solution for harnessing solar energy and integrating it with thermal storage for high-enthalpy applications, such as electricity generation and industrial heating [1,2]. Thermal CSP is projected to contribute up to 11% of global electricity generation by 2050, with an expected output of 180 TWh by 2030 [3]. The use of Solar Salt (60% $NaNO_3$, 40% KNO_3) in a two-tank configuration for sensible heat storage (SHS) is one of the most widely adopted technologies owing to its excellent thermal properties and cost-effectiveness [4].

Although there is a relatively extensive body of literature on the flow and heat transfer of molten salt and the thermal efficiency of TES tanks, research on the thermal and mechanical properties of molten salt storage tank bodies is limited. Recently, a report by Ref. [5]investigated the failure mechanisms of commercial-scale molten salt TES tanks used in central receiver CSP plants. In addition, a recent collaborative study proposed a multi-physics 2-D model that focuses on the mechanical and thermal mechanisms of the storage tank body, utilizing the tank structure and operational data from the latest commercialized CSP plants [6].

From a materials perspective, the operating conditions are very harsh, especially for the hot storage tank in the two-tank configuration, with a maximum operating temperature of 560 °C. Mechanical and thermal stresses and Solar Salt in contact with the tank wall and floor are operational conditions that are not fully considered in the API code used for tank design. Austenitic steels have been proposed as structural materials for constructing hot storage tanks. The motivation of this study is to analyze the different failure modes and causes of these alloys in severe

☆ The authors collectively possess strong expertise in the fields of high-temperature material performance, molten salt corrosion, and thermal energy storage systems. Sergio A. Ardila Parra is a predoctoral researcher at the University of Barcelona specializing in creep and corrosion behavior of austenitic steels in molten salts within CSP applications. Dr. Cristina Prieto (former R + D director in Abengoa Solar and now Associate Professor at Universidad de Sevilla) has an extensive track record in molten salt formulation, corrosion mechanisms, and thermal storage system integration for concentrating solar power. Dr. Julian D. Osorio (NREL, USA) contributes recognized experience in high-temperature components and reliability assessment for energy systems. The corresponding author, Prof. Ana Inés Fernández (University of Barcelona), is internationally known for her leadership in materials for thermal energy storage, with numerous peer-reviewed publications and the coordination of national and European research projects. Together, the team provides complementary expertise and demonstrates an impact directly aligned with the scope of the review.

* Corresponding author.
E-mail address: ana_inesfernandez@ub.edu (A.I. Fernández).

https://doi.org/10.1016/j.jmrt.2026.02.207
Received 1 December 2025; Received in revised form 2 February 2026; Accepted 24 February 2026
Available online 26 February 2026

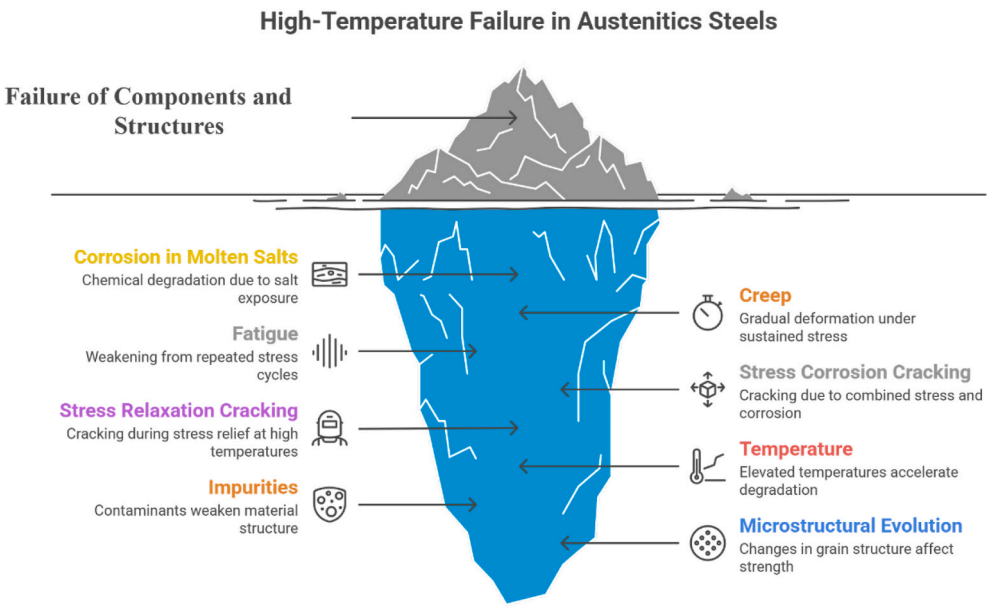

Fig. 1. Factors involved in the failure of austenitic stainless steel.

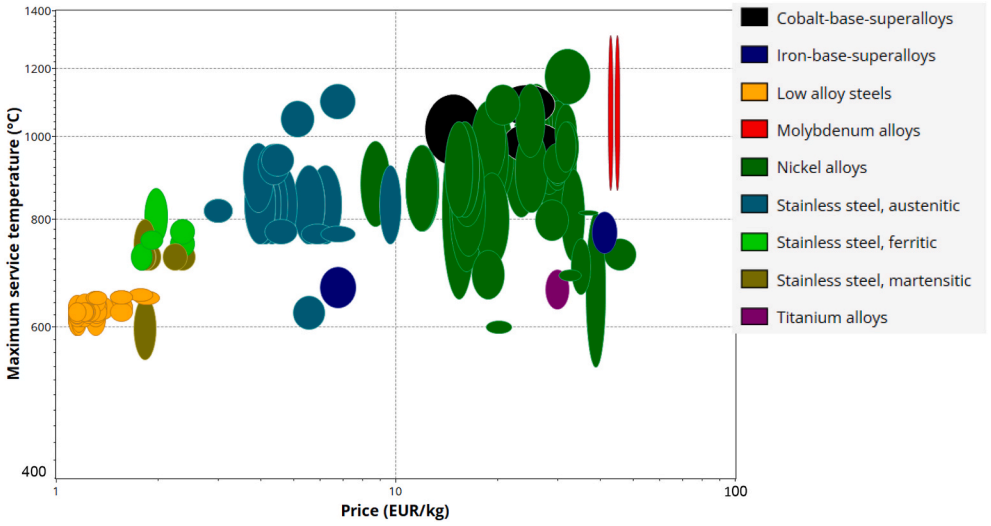

Fig. 2. Comparison of different materials for high-temperature services.

environments to better understand the multi-objective design requirements that must be satisfied for long-term applications. Fig. 1 presents an iceberg-based schematic emphasizing that the failure of components and structures in austenitic stainless steels at high temperatures is often only the visible manifestation of deeper, less apparent factors. These include material composition, microstructural stability, environmental exposure, and thermomechanical conditions, which collectively control degradation and failure. The remainder of this paper is organized as follows: first, a description of the composition of austenitic steels is presented, followed by a detailed analysis of each failure mode.

1.1. Austenitic steel composition and the role of alloying elements

Austenitic steels are formed by a phase composed of a face-centered cubic (FCC) crystalline structure that provides high ductility, toughness, and weldability. A high chromium composition provides high corrosion resistance and helps stabilize the austenite phase at room temperature, whereas nickel improves ductility and toughness and contributes to corrosion resistance [7]. Small amounts of carbon improve strength through carbide formation; however, between 400 °C and 900 °C, carbon may form chrome carbides in grain boundaries, reducing the availability of chrome to create a passive layer of chrome oxide and increasing the probability of intergranular cracking in a phenomenon called sensitization [8]. The addition of manganese improves toughness and can partially replace nickel to stabilize austenite. Molybdenum increases the resistance to pitting, cracking, and creep, which is essential for preventing failure at high ambient temperatures. Lastly, Niobium helps to prevent chrome carbide formation by forming carbides with carbon; these carbides act as reinforcement, increasing the strength of the steel (precipitation strengthening) [9]. However, negative effects on welds and the presence of stress relaxation cracking (SRC) have been reported in several studies [10–12].

The ANSYS Selector software includes the maximum service temperature as a parameter for guiding the material selection. The maximum service temperature is defined as the temperature at which a material can withstand extended periods without significant degradation of its properties. Fig. 2 compares the approximate service

Table 1
Chemical compositions of several austenitic stainless steels (*wt%*).

Steel Grade	Cr	Ni	C	Mn	Si	Mo	Nb (Cb)	Ti	N	Fe (bal.)
AISI 304	18–20	8–10	≤0.08	≤2.0	≤1.0	—	—	—	—	~70
AISI 316	16–18	10–14	≤0.08	≤2.0	≤1.0	2–3	—	—	—	~65
AISI 316L	16–18	10–14	≤0.03	≤2.0	≤1.0	2–3	—	—	—	~65
AISI 321	17–19	9–12	≤0.08	≤2.0	≤1.0	—	—	≥5xC	—	~70
AISI 347	17–20	9–13	≤0.08	≤2.0	≤1.0	—	≥10xC	—	—	~68
AISI 347H	17–20	9–13	0.04–0.10	≤2.0	≤1.0	—	≥10xC	—	—	~68
AISI 800H	19–23	30–35	≤0.10	≤1.5	≤1.0	—	—	—	—	~45

temperature and relative cost of various structural materials after implementing the following restrictions:

- Metals and alloys for a maximum service temperature range from 500 to 1300 °C
- Limited to processing technologies: acceptable and excellent for hot and cold metal forming.
- Not susceptible to stress corrosion cracking

Each bubble represents the grade of a specific material. The size of the bubble represents the property analyzed from the supplier's technical data. Austenitic stainless steels, such as AISI 347H, are favorable owing to their excellent balance of high-temperature strength, corrosion resistance, and economic viability. While martensitic and ferritic steels are more cost-effective, their limited resistance to high-temperature oxidation and reduced creep performance [8] make them less suitable for prolonged use in molten salt environments typical of Concentrated Solar Power (CSP) systems. Similarly, while nickel-based superalloys demonstrate exceptional high-temperature properties, their high cost and limited availability make austenitic stainless steels, such as AISI 347H and 316L, a more economically viable option for large-scale molten salt storage tanks. These steels provide a suitable combination of high-temperature performance, corrosion resistance, and weldability, rendering them attractive for concentrated solar power (CSP) applications.

Austenitic stainless steels are among the most studied materials for high-temperature applications in CSP systems because of their excellent corrosion resistance, mechanical stability, and oxidation. Table 1 summarizes the nominal chemical compositions of austenitic stainless steels frequently evaluated or utilized in molten salt and high-temperature environments relevant to CSP operations.

2. Failure modes and mechanisms at high temperature

At high temperatures, corrosion is one of the most studied failure modes, where the thickness of the component walls is reduced, resulting in mechanical failures. Lai [13] considers an application of high temperature when most reactions and chemical changes occur; this temperature is about 500 °C. However, this study also mentioned several reports showing severe damage in applications with service temperatures ranging from 260 to 315 °C. To cover a broad and diverse group of failures and analyses, temperatures of approximately 250 °C were considered in this review. Corrosion can occur uniformly through the granular surface, intergranular, pitting, and by the combined presence of a corrosive atmosphere and mechanical stresses, that is, stress-corrosion cracking (SCC) [14]. Fatigue failure has also been studied owing to fluctuations in the temperature field in principal applications, and variations in mechanical properties can also occur [15]. Creep is the permanent deformation produced by stresses lower than the yield strength limit, and this failure mode is typical in storage tanks, where high pressures and temperatures are present [16]. Finally, austenitic steel fails by sensitization at high temperatures, causing intergranular cracking (IGC) and the formation of carbides, nitrides, or sigma phases in the grain boundary, thereby weakening the material. The mechanisms underlying these failure modes (Creep and IGC) can be summarized as follows: (1) atomic diffusion, in which atoms can diffuse in grain boundaries, facilitating precipitate formation, (2) decomposition of the austenite phase occurs at high temperatures when the arising sigma phase or chrome carbides provoke intergranular cracking, (3) oxidation occurs when layers of oxides appear after long steel exposures at high temperatures [17], and (4) high temperatures facilitate dislocation glide. Thus, the material deforms plastically under a constant load, causing creep.

Table 2
Relative relevance of failure mechanisms for austenitic stainless steels in CSP molten-salt.

Failure mechanism	Relevance in CSP tanks	Primary drivers	Typical location
Stress relaxation cracking (SRC)	Very High	Residual welding stresses, long-term exposure at 500–650 °C, HAZ sensitization	Welded joints (tank bottom, vertical seams)
Creep–corrosion interaction	High	Constant load and molten salt corrosion, microstructural degradation	Load-bearing plates, near welds
Thermal fatigue/ thermo-mechanical fatigue	High	Daily thermal cycling, temperature gradients	Tank bottom, nozzles
Uniform corrosion	Medium	Salt chemistry, impurities, exposure time	General surface
Localized corrosion (pitting/IGC)	Medium–Low	Chloride impurities, redox imbalance	Near-surface, grain boundaries
Classical SCC	Low	Low applied stress, limited aqueous conditions	Secondary relevance

Before investigating the various degradation mechanisms that may affect the components of large molten salt storage tanks, it is essential to assess their significance under service conditions. Recent operational experience indicates that not all failure modes contribute equally to the degradation of components within a Concentrated Solar Power (CSP) plant. The primary factors affecting the long-term structural integrity of these components at approximately 560 °C include stress relaxation cracks (SRC) forming in the heat-affected zone due to post-weld heat treatment, the interaction between creep and the corroded load on the structure, and the cyclic loading effects resulting from significant daily temperature fluctuations. These degradation mechanisms are classified as primary; however, numerous other mechanisms, such as classical stress–corrosion cracking (SCC) or uniform corrosion, may also be involved. The failure mechanisms of stainless steels in CSP, along with their relevance and specific locations within CSP components, are detailed in Table 2.

2.1. Corrosion

2.1.1. Uniform corrosion

This subsection investigates the general corrosion behavior of several

alloys in high-temperature environments and establishes a baseline for comparing the relative corrosion rates. Uniform corrosion in austenitic steels at high temperatures is often described by the progressive loss of protective layers and degradation of the alloy matrices [18]. Studies have consistently reported the formation of duplex oxide structures with an outer Fe-rich layer and an inner Cr–Ni-rich layer [19]. However, although this bilayer morphology is recurrent, its stability strongly depends on environmental conditions. For instance, carburization and nitridation tend to accelerate vacancy formation and precipitation-driven stresses [20,21], suggesting that microstructural degradation is a function of oxidation and the ingress of interstitial elements. Thus, although the general mechanism is well-established, the rate and severity differ according to the gas composition, temperature, and prior alloy processing.

- Corrosion in different gas environments

In aqueous and steam environments, the uniform corrosion of austenitic stainless steels is primarily driven by electrochemical reactions and the development of hydrated oxide layers. These oxide films typically feature an outer iron-rich layer (Fe_2O_3 or Fe_3O_4) and an inner chromium-enriched layer (Cr_2O_3 or spinel-type oxides), with their protective qualities depending on oxygen availability, temperature, and transport through the oxide. In high-temperature gaseous environments, corrosion is governed by solid-state diffusion and oxidation kinetics, where chromium activity and oxygen partial pressure dictate the stability and growth rate of protective oxide scales.

Comparative analyses of petrochemical applications have revealed important differences. In HK40 steel, sulfide-containing gases induce catastrophic leakage failures [22], whereas in oxidizing–sulfurizing atmospheres, HR160 specimens mainly exhibit scale growth without immediate rupture [23]. This suggests that sulfides accelerate localized damage more severely than mixed oxidizing gases. Similarly, in H2–H2O atmospheres, a cubic dependence of oxidation on the oxygen partial pressure was observed in HK40 [24], and tubes made of HK40 also failed owing to oxidation and time-dependent cracking [25]. Other investigations on ethylene pyrolysis have shown more complex oxide stratification [26], indicating that the oxide morphology and kinetics can diverge even in similar industrial settings.

Long-term exposures also highlight discrepancies: Inconel 601 in a methanol plant operating at 560° °C developed deep $M_{23}C_6$ carbides after two years at 560 °C [27]. In contrast to the corrosion resistance comparison between austenitic HR-160 and HA-188, HR-188 showed a poor weight change, which was probably due to the slower diffusion of chromium [28]. The mass gain in several austenitic steels and nickel alloys (AISI 304, AISI 316L, IN625, and IN690) after exposure to supercritical water at temperatures from 400 °C to 550 °C has been reported by several authors [29,30], the results showed that alloys 690 and 625 present superior corrosion resistance (based on mass gain and oxide thickness), and AISI 304 is slightly better than AISI 316L; however, economic analysis was not performed, which can be decisive in material selection studies. A study using vapor at 600 °C for 1500 h compared two different austenitic steel sheets (Fe–21Cr–32Ni and Fe–17Cr–9Ni), resulting in better corrosion resistance in an alloy with a higher Cr and Ni content. The Cr content was sufficient to support a continuous chromium layer at the oxidation front. These results were supported using advanced characterization techniques that helped analyze the five oxide scales formed on the steel surface [31].

Other studies have implemented novel methods to evaluate corrosion; for example, AISI 304 was analyzed in water at 100 °C and 250 °C using electrochemical noise, identifying two main stages: passive and active dissolution of the protective layer [32]. In contrast to other failure modes with HR3C steel in steam at 700 °C, cracking and buckling dominated rather than corrosion. It was found that the chromium concentration was sufficient to maintain a protective layer; however, mechanisms such as the accumulation of molecular hydrogen in the pores can lead to cracking [33]. Some studies have focused on approaches and materials for reducing corrosion damage. A thermomechanical process was proposed to lessen corrosion in AISI 316L under supercritical water at 600 °C and 25 MPa; the thickness of the hot-rolled stainless steel was reduced by up to 90%, reaching a reduction of approximately four times the weight of the oxide layers [34].

In the new generation of nuclear power plants, lead melt is a promising coolant; the corrosion rate of AISI 310 in contact with lead melt was investigated, and it was found that the molten lead at 450 °C does not penetrate deep into a matrix formed by a two-layer structure, whereas molten lead combines with some alloy elements next to the base metal [35]; AISI 316H was also evaluated for the same application with a similar coolant. It was observed that a high percentage of cesium (~5%) could drastically affect the corrosion behavior at 600 °C [36]. Such comparisons underscore that time-dependent carbide precipitation and stress-driven degradation can be as damaging as the surface oxidation. Furthermore, the alloy composition strongly modulates its performance. Outokumpu 253 MA variants with different Cr, Si, and Ce contents displayed markedly different oxide growth after 100 h at 750–1100 °C [37], whereas fine-grained AISI 321 exhibited enhanced Cr-rich oxide formation relative to coarse-grained microstructures [38]. The effect of the aging process was analyzed for AISI 304H and H3C during oxidation under steam at 650 °C. Specimens with higher Cr contents were significantly improved, and the mass gain was reduced [39].

Surface condition is another critical factor in assessing the corrosion resistance. Polished AISI 304L produced thicker Cr-rich oxides than ground surfaces after 500 h at 400 °C in steam [40], and pickling and shot peening (SP) promoted the stability of Cr_2O_3 and $FeCr_2O_4$ scales in AISI 304H in steam at 700 °C [41,42]. These findings suggest that pretreatment can shift the corrosion behavior as much as alloying. Finally, advanced alloys, such as alumina-forming austenitic (AFA) alloys, have outperformed conventional grades in both solar salt [43] and supercritical CO2 [44] applications. In addition, sodium carbonate coatings were assessed to improve the corrosion resistance of AISI 330 and AISI 330CB at service temperatures up to 900 °C in a nitrogen-hydrogen atmosphere. The results showed a significant reduction in mass gain in the coated samples [45], indicating the need for future design strategies beyond the conventional Cr–Ni balancing. Research conducted in high-temperature aqueous environments has revealed that corrosion resistance does not consistently increase with the chromium content. For example, recent investigations into FeCrAl alloys in PWR water have demonstrated enhanced protection of alloys with lower chromium content. This can be attributed to variations in the oxide nucleation and growth mechanisms, emphasizing the significance of early-stage oxidation kinetics over the bulk composition alone. Although these studies were conducted in aqueous environments, the mechanistic insights gained are pertinent to understanding the corrosion trends observed in molten salts [46].

- Corrosion in molten salt environments

In molten salt systems, uniform corrosion is significantly affected by salt chemistry, redox potential, and impurity content (e.g., chlorides or moisture). Oxide formation may be restricted or destabilized due to low oxygen activity, dissolution of oxide species into the melt, or chemical interactions between molten salts and alloying elements. Consequently, corrosion can progress through a combination of non-protective oxide formation and accelerated metal dissolution, resulting in higher apparent corrosion rates even when the surface morphology remains macroscopically uniform. These mechanisms are particularly pertinent for CSP thermal energy storage tanks operating at 560–600 °C.

API 650 [47] and ASME Section VIII Div 1 [48] dictate the relevant standards for material selection, wall thickness, and safety factors for thermal and mechanical loads in CSP plants. These standards also describe the auxiliary tanks. The structurally stable and highly tempered

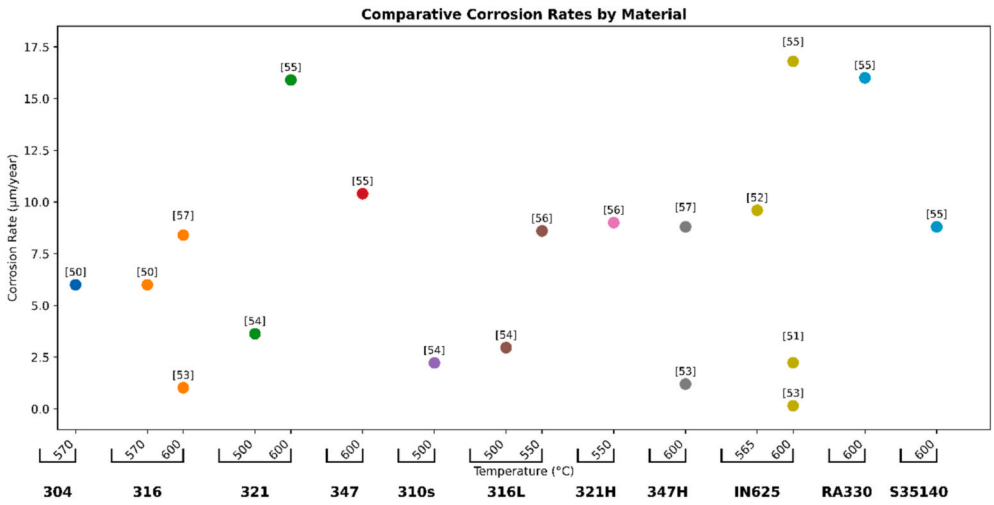

Fig. 3. Corrosion rates of different austenitic stainless steels under solar salt at various temperatures, measured in mm/year.

austenitic stainless steel AISI 347H is routinely used because of its architectural robustness and heat-induced corrosion resistance. The occurrence of molten-salt corrosion in these systems is hazardous. Although solar salts (nitrates) are less corrosive than chlorides, metallic impurities combined with thermal cycling can cause localized or generalized corrosion. To counter such occurrences, design restrictions have been established to limit the number of chlorides and the moisture content. In addition to protective coatings or inert gas blanketing, testing procedures such as ASTM G111 [49] have been implemented.

Initial studies compared the corrosion of different materials and salt impurities. AISI 304 and AISI 316 were assessed in *solar salt* at 560 °C, and the results showed low corrosion rates (6-15 µm y^{-1}); there was a strong influence of chloride concentration on the corrosion resistance of AISI 304 [50]. Subsequently, the corrosion behavior of AISI 316, AISI 347H, INCONEL 625, and other 2 proposed materials in *solar salt* at 600 °C for 500 h was analyzed. The results showed similar behavior for AISI 316 and AISI 347H (0.4-0.6 mg/cm^{-2}) and an outstanding performance of IN625 (~0 mg/cm^{-2}); however, again, it is not an economic aspect related. Also, recent studies with experiments at longer exposure times of 4000 h and 1470 h, in solar salts place the corrosion rate of IN625 at 2.23 and 9.6 µm y^{-1}, respectively [51–53]. The initial stage of the corrosion mechanism of austenitic steels immersed in quaternary molten salt at a high temperature is controlled by the corrosion reaction, according to the investigation of Wang et al. [54], where AISI 310S, AISI 316L, and AISI 321 were assessed at 500 °C. Subsequently, a diffusion-controlled process dominated the growth of the oxide layer, where the formation rate decreased as the oxide film thickened. The results indicated that AISI 310S had the best corrosion resistance, with a rate of only 2.22 µm y^{-1}, owing to its higher chromium content. Fig. 3 presents a comparative study of the corrosion rates of different alloys used in structures when exposed to molten salts at high-temperature settings. Despite a certain level of variation in values based on variations in the type of compounds used in salts, exposure time, and differing methods of tests, a certain trend emerges at 600 °C in particular when austenitic and-stainless AISI 316 and AISI 347H possess a substantially low rate of corrosion compared with a number of different options available, whereas some of them are very comparable to Inconel 625 with a high price being a certain advantage. This makes 316 and 347H remain actual options among a number of different candidates available for use in CSP hot tanks operating within a 560–600 °C range, pending reliable management of impurities and a degradation mechanism within a certain timeframe.

In molten nitrate salts, most studies converge on moderate but non-negligible uniform corrosion rates (≈8–9 µm y^{-1} for AISI 316L, 321H, and 347H at 550–600 °C) [55–57]. However, discrepancies emerge under thermal cycling: Bradshaw and Goods [58] reported up to 50% higher corrosion rates compared with isothermal conditions in AISI 316L and AISI 304 in solar salt, while Shi et al. [59]showed that tribological exposure further thickens oxide scales in AISI 316H. Thus, static immersion tests may underestimate degradation under real CSP operating conditions.

Other molten salts, rather than nitrate solar salt, have been used, and the corrosion of several alloys was studied. A comparison between austenitic and ferritic proposed steels in terms of corrosion was conducted in a eutectic molten salt composed of (Na, K) NO_3 mixture at different temperatures (400 °C – 600 °C). The results were presented in terms of the activation energy of the corrosion process and showed slightly better behavior for ferritic steels, a process that is highly dominated by diffusion mechanisms [60]. Other studies have sought to identify the best techniques and procedures for conducting reliable corrosion measurements. Two corrosion measurement techniques were implemented to assess AISI 309 in Na_2SO_4 molten salt at 700 °C and 600 °C. This study compared the electrochemical technique with the weight loss method. The results showed higher corrosion rates using the conventional weight-loss method, likely because of the excessive cleaning [61]. The corrosion behavior of high and low-carbon alloys (AISI 304, AISI 316L, AISI 347, 310S and DIN X5NiCrNbCe32-27, DIN X20 CrMoV12-1(AISI 422, UNS S42200), DIN X12CrCoNi17-12-2, 10CrMo9-10 (AISI 335 Gr. P22, UNS K21590), and Inconel 690) were compared under molten carbonate fuel cell conditions at 650 °C, and alloys with different chromium compositions were analyzed; the 17 wt % Cr showed the best choice for this application [62]. Dynamic corrosion assessments of austenitic stainless steels (AISI 304, 316L, and 347H) in binary nitrate-carbonate molten salts at 600 °C, over a duration of 1000 h demonstrated a distinct correlation between corrosion rate and both alloy composition and flow conditions [63]. Utilizing weight loss measurements, the corrosion rates at a flow rate of 2 m/s were determined to be 0.0217, 0.0122, and 0.0076 mm y^{-1} for 304, 316L, and 347H, respectively, which are 3–4 times higher than those observed under static conditions. XRD, SEM, and EDS analyses identified iron oxides as the predominant corrosion products. The enhanced corrosion resistance of 316L compared to 304 is attributed to its Cr and Ni content, while the Nb and Ni additions in 347H further augment its stability under dynamic conditions. These findings underscore the significance of alloying and flow conditions in managing the high-temperature molten salt corrosion of austenitic stainless steels. The thermal stability and corrosion performance of a low-melting-point ternary hybrid molten salt were assessed at 600 °C. The salt exhibited acceptable thermophysical properties; however, it experienced significant degradation after prolonged exposure. Static corrosion tests conducted on AISI 304 and 316

Table 3
Corrosion rates of several austenitic stainless steels.

Material	Salt Type	Temperature	Corrosion rate	Units	Time (hours)	Commentaries	Author
AISI 310S	KNO_3–$NaNO_2$–$NaNO_3$–KCl	500	2.22	μm y^{-1}	1008	SC, WL	W. Wang et al., 2019
AISI 316L	KNO_3–$NaNO_2$–$NaNO_3$–KCl	500	2.96	μm y^{-1}	1008	SC, WL	W. Wang et al., 2019
AISI 321	KNO_3–$NaNO_2$–$NaNO_3$-KC_L	500	3.63	μm y^{-1}	1008	SC, WL	W. Wang et al., 2019
AISI316	60% $NaNO_3$ - 40% KNO_3	570	6-15	μm y^{-1}	7000	SC, WL	Goods & Bradshaw, 2004
AISI 304	60% $NaNO_3$ - 40% KNO_3	570	6-15	μm y^{-1}	7000	SC, WL	Goods & Bradshaw, 2005
AISI 316	60% $NaNO_3$ - 40% KNO_3	600	1.02	μm y^{-1}	5000	SC, WL	Soleimani Dorcheh et al., 2016
AISI 347H	60% $NaNO_3$ - 40% KNO_3	600	1.22	μm y^{-1}	5000	SC, WL	Soleimani Dorcheh et al., 2016
IN 625	60% $NaNO_3$ - 40% KNO_3	600	0.15	μm y^{-1}	5000	SC, WL	Soleimani Dorcheh et al., 2016
IN 625	60% $NaNO_3$ - 40% KNO_3	600	16.8	μm y^{-1}	3000	SC, WL	Kruizenga et al., 2013
AISI 321	60% $NaNO_3$ - 40% KNO_3	600	15.9	μm y^{-1}	3000	SC, WL	Kruizenga et al., 2013
AISI 347	60% $NaNO_3$ - 40% KNO_3	600	10.4	μm y^{-1}	3000	SC, WL	Kruizenga et al., 2013
253 MA	60% $NaNO_3$ - 40% KNO_3	600	38.6	μm y^{-1}	3000	SC, WL	Kruizenga et al., 2013
RA330	60% $NaNO_3$ - 40% KNO_3	600	16	μm y^{-1}	3000	SC, WL	Kruizenga et al., 2013
UNS S35140	60% $NaNO_3$ - 40% KNO_3	600	8.8	μm y^{-1}	3000	SC, WL	Kruizenga et al., 2013
AISI 316	60% $NaNO_3$ - 40% KNO_3	600	8.4	μm y^{-1}	3000	SC, WL	Trent et al., 2016
AISI 347H	60% $NaNO_3$ - 40% KNO_3	600	8.8	μm y^{-1}	3000	SC, WL	Trent et al., 2016
IN 625	60% $NaNO_3$ - 40% KNO_3	600	2.23	μm y^{-1}	4000	SC, WL	Elbakhshwan et al., 2022
IN 625	60% $NaNO_3$ - 40% KNO_3	565	9.6	μm y^{-1}	1470	SC, WL	Prieto et al., 2022
AISI 309	50% Na2SO4 - 50% V2O5	700	2530	μm y^{-1}	120	SC, WL, EC	Cuevas Arteaga, 2012
AISI 316	60% NaNO3 - 40% KNO_3 -0.05Cl	565	8.98	μm y^{-1}	4584	SC, WL, TC	Bradshaw & Goods, 2001
AISI 316L	60% NaNO3 - 40% KNO_3-0.05CL	565	8.41	μm y^{-1}	4584	SC, WL, TC	Bradshaw & Goods, 2001
AISI 304	60% NaNO3 - 40% KNO_3-0.05Cl	565	11.47	μm y^{-1}	4584	SC, WL, TC	Bradshaw & Goods, 2001
AISI 347H	24.5% NaCl - 8.2% KCl-67.3% $CaCl_2$.	600	2383.628	μm y^{-1}	400	SC, WL	Xiao et al., 2025
IN 625	24.5% NaCl - 8.2% KCl-67.3% $CaCl_2$.	600	5437.520	μm y^{-1}	400	SC, WL	Xiao et al., 2025
Haynes 230	24.5% NaCl - 8.2% KCl-67.3% $CaCl_2$.	600	487.639	μm y^{-1}	400	SC, WL	Xiao et al., 2025
AISI 304	$NaNO_3$–Na_2CO_3	600	21.7	μm y^{-1}	1000	DC, WL	Wang et al., 2025
AISI 316L	$NaNO_3$–Na_2CO_3	600	12.2	μm y^{-1}	1000	DC, WL	Wang et al., 2025
AISI 347H	$NaNO_3$–Na_2CO_3	600	7.6	μm y^{-1}	1000	DC, WL	Wang et al., 2025

Abbreviations: SC = static corrosion, DC = dynamic corrosion EC = electrochemical testing; WL = weight loss measurement.

stainless steels demonstrated measurable mass loss after 1000 h, corresponding to an annual corrosion rate of approximately 0.07 mm y^{-1}. These findings underscore that even thermally stable salt formulations can cause notable corrosion in conventional austenitic steels under conditions relevant to concentrated solar power (CSP) applications [64]. Furthermore, Static corrosion tests have demonstrated that the corrosion rate of AISI 316 increases consistently with the Na_2CO_3 content. This finding confirms that while salt additives may enhance thermal performance, they can negatively impact material durability in molten salt systems relevant to concentrated solar power (CSP) [65].

Nonetheless, aggressive salts such as $NaVO_3$ at 700 °C still reveal significant vulnerability, even in high-Ni steels such as AISI 309 and AISI 310 [66]. Additive effects can be dramatic: 5% V_2O_5 additions to a eutectic mixture of molten salts, Na_2SO_4 and NaCl (75 – 25 wt%), increased the corrosion of AISI 304H at 800–900 °C by up to approximately 250% in terms of mass change [67], underscoring that minor compositional changes in salts may dominate over alloy selection. Recently, novel molten salt formulations have been proposed for implementing the Brayton cycle in third-generation CSP systems operating at temperatures of up to 700 °C. One study compared the corrosion resistance of Haynes 230, AISI 347H, and Inconel 625 in a molten chloride mixture composed of 24.5 wt % NaCl, 8.2 wt % KCl, and 67.3 wt % $CaCl_2$. The results showed that Haynes 230 exhibited the best corrosion resistance, with a corrosion rate of 487.639 μm y^{-1}, whereas AISI 347H and Inconel 625 exhibited higher rates of 2383.628 μm y^{-1} and 5437.520 μm y^{-1}, respectively, after 400 h of exposure [68].

The corrosion rate data presented in Table 3 are derived from studies conducted under significantly varied experimental conditions, encompassing differences in exposure duration, salt purity, chloride contamination, temperature, and testing methodologies. Although the referenced authors provide detailed experimental procedures, direct quantitative comparison of corrosion rates remains challenging. Short-term tests may overestimate corrosion rates due to transient oxidation, whereas long-term exposures are more likely to reflect stabilized corrosion kinetics. Furthermore, static immersion tests typically produce different corrosion behaviors compared to dynamic or flowing salt

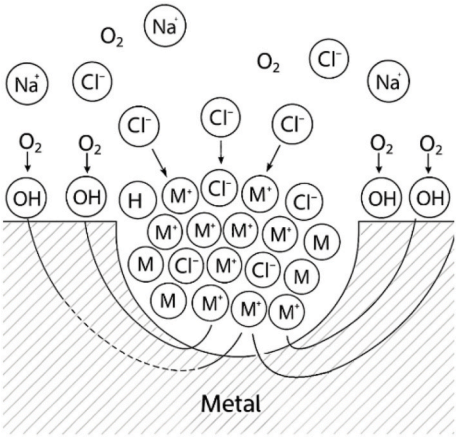

Fig. 4. Left: Schematic representation of pitting process.

conditions. Consequently, the values in Table 3 should be interpreted as indicative trends rather than definitive rankings for material selection.

Although a broad spectrum of corrosion rates has been reported, direct comparisons between studies are complicated by variations in salt chemistry, impurity levels, exposure duration, and testing methods. These inconsistencies underscore the necessity of standardized testing protocols under conditions relevant to concentrated solar power (CSP).

2.1.2. *Pitting*

This section focuses on localized pitting corrosion, emphasizing the influence of alloy composition, protective oxide formation, and operating conditions on pit initiation and propagation. Pitting corrosion, characterized by the localized breakdown of passive films, is typically associated with halide-rich aqueous environments rather than high-temperature molten salts [69]. A key descriptor of this process is the Critical Pitting Temperature (CPT), below which pits remain unstable, and above which the pitting potential decreases linearly with

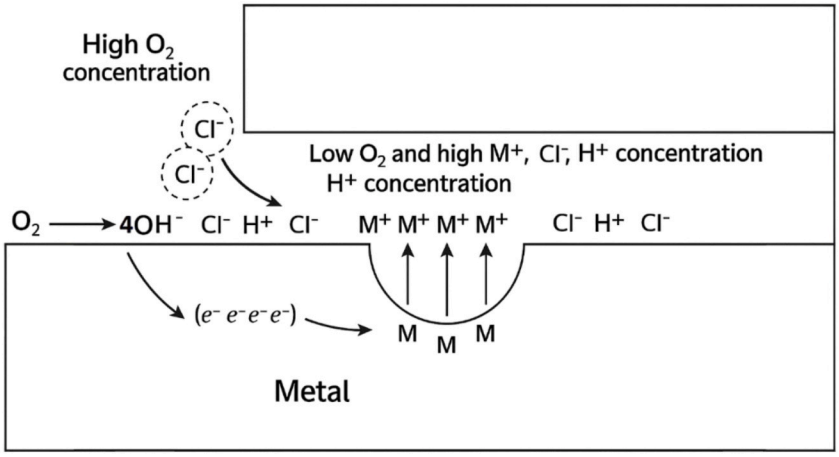

Fig. 5. Schematic representation of the crevice mechanism.

temperature [70,71]. For AISI 304, the reported CPT values range from 150 to 200 °C, with the pitting susceptibility increasing as the temperature increases in aerated chloride solutions [72]. Interestingly, above 220 °C, the oxide film became more stable, limiting ionic transport and suppressing stable pit growth, as shown in Fig. 4. Fig. 4 provides a schematic representation of the pitting corrosion mechanism on an austenitic stainless steel surface. It emphasizes the interaction between the base metal and aggressive species such as Cl^- ions, alongside the presence of Na^+, metal cations and anions (M^+/M^-), OH^-, and dissolved oxygen (O_2).This apparent reversal highlights the complex role of temperature, which promotes pitting in the intermediate regime but may enhance passivity at even higher levels (see Fig. 5).

The role of reaction kinetics in pit initiation has also been discussed. Manning et al. [73], who studied AISI 304L in deionized water with 100 ppm chloride ions, concluded that adsorption-related kinetics dominate at elevated temperatures, suggesting that film breakdown may not be purely electrochemical but also linked to surface chemistry and adsorption dynamics.

In contrast, localized attacks are far less dominant in molten salt environments. Dorcheh et al. [53], investigating AISI 347H in solar salt at 600 °C, reported the formation of multiphase oxide scales containing Fe oxides, Na-ferrites, and Fe–Cr spinels, with uniform scale growth outweighing localized penetration. This suggests that pitting is largely suppressed under molten salt conditions, where ionic transport and diffusion-controlled oxide growth dictate corrosion, whereas aqueous chlorides remain the most critical scenarios for pit initiation and propagation.

2.1.3. Crevice corrosion

This section addresses crevice corrosion, which can occur in shielded areas or tight gaps. Factors such as chloride accumulation, temperature, and alloy microstructure were discussed to assess the susceptibility of the materials studied. Crevice corrosion develops in shielded regions, where restricted mass transport alters the local chemistry [74]. The process is typically driven by anodic metal ionization and a shift in cathodic kinetics, which makes alloys with anodic control more vulnerable [75,76]. While oxygen availability can modulate the severity of an attack, most studies emphasize that pH reduction inside the crevice is the dominant factor [77,78]. Early electrochemical models, such as those proposed by Betts and Boulton [79], established a framework of reduction reactions that still underpins mechanistic understanding. A schematic representation of the crevice mechanisms is shown in Fig. 5.

Practical failures reinforce these mechanisms. Kaul et al. [80] reported crevice corrosion in AISI 304 heat exchanger tubes operating with syngas at 126–163 °C, where crevice formation at tube-to-tube sheet gaps promoted local acidification. At higher temperatures, the interplay between the other degradation modes becomes evident. Saito et al. [81] observed that intergranular stress corrosion cracking accelerates crevice processes in AISI 304 at 280 °C water, highlighting the synergistic effects between localized corrosion and cracking mechanisms.

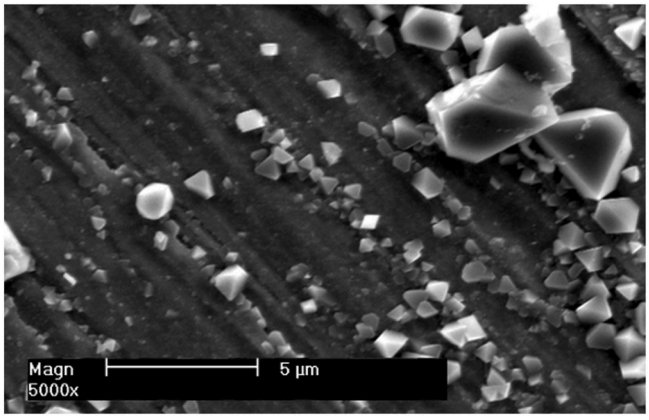

Fig. 6. Crevice morphology of AISI 304 [83].

However, not all environments follow the same pathway. In Inconel 600, studies at 288 °C water revealed that the classical film rupture theory of stress corrosion cracking does not govern crevice corrosion; instead, aqueous diffusion inside the gap controls the corrosion rate [82]. Chen et al. [83] further refined this view by showing that crevice geometry is decisive: width primarily dictates dissolved oxygen concentration, while length strongly influences pH within the occluded zone. These conclusions were drawn from the analysis of AISI 304 stainless steel immersed in vapor at 290 °C.

Thermal effects on passivity also play significant roles. Trasatti et al. [84] demonstrated that surface heating in AISI 304L at 150–300 °C weakens passive film stability, enhancing nucleation of localized attack. This suggests that industrial processes such as welding, brazing, and sterilization can predispose stainless steels to crevice corrosion even before they are exposed to service conditions.

Overall, the literature shows broad agreement that pH gradients within the crevice drive corrosion, but the severity depends on the alloy composition [74–76], geometry [83], and additional factors such as stress [81] or surface thermal history [84]. The differences across alloys (e.g., AISI 304 vs. Inconel 600) also indicate that a single mechanistic model may not fully capture crevice corrosion in all high-temperature aqueous systems. The crevice morphology of AISI 304 showed in Fig. 6 displays characteristic crystalline corrosion products indicative of

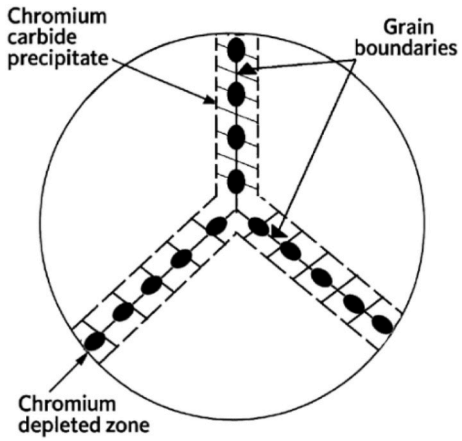

Fig. 7. Representation of grain boundaries in sensitized AISI 304.

localized dissolution within the crevice [83].

In addition to environmentally induced localized corrosion mechanisms such as pitting and crevice corrosion, extended exposure to high temperatures and thermal cycles associated with welding can lead to microstructural alterations, particularly sensitization, which significantly influence intergranular corrosion behavior.

2.1.4. Sensitization and intergranular corrosion

Finally, we examined sensitization and intergranular corrosion, highlighting how welding, heat treatments, and alloying elements affect chromium depletion along the grain boundaries and the subsequent corrosion susceptibility (see Fig. 6). In austenitic stainless steels, sensitization refers to the precipitation of chromium carbides at grain boundaries within the 500–800 °C temperature range [85]. This process involves the rapid diffusion of interstitial carbon to the boundaries, where carbides nucleate and deplete the adjacent chromium regions [86,87]. Consequently, these depleted zones lose passivity and become preferential sites for intergranular attacks. Fig. 7 shows a schematic representation of the microstructural characteristics of sensitized austenitic stainless steel, emphasizing the precipitation of chromium carbides along the grain boundaries and the resultant chromium-depleted zones that facilitate intergranular degradation. The formation of sensitized microstructures is governed by the interplay between carbide precipitation thermodynamics and chromium diffusion kinetics [88,89], indicating that both the alloy chemistry and thermal history dictate the susceptibility.

Comparative evaluations across different grades reinforce this dependence. Lima et al. [90] systematically examined the critical sensitization temperature in AISI 304L, 316L, 321, and 347. Their results showed that none of the alloys were sensitized at 380 °C, but above 500 °C, all except AISI 347 developed chromium-depleted boundaries. For AISI 347, stabilization through niobium addition delayed carbide precipitation, shifting the critical temperature closer to 550 °C. This highlights how alloying strategies (e.g., Nb or Ti stabilization) can markedly mitigate sensitization, in contrast to unstabilized grades such as 304L or 316L.

Taken together, the literature converges on the view that sensitization is unavoidable once steels are exposed to the 500–800 °C window for a sufficient time; however, the critical threshold varies with composition. Although chromium diffusion kinetics set the general boundary, alloy design, particularly carbide stabilizers, provides the most effective resistance against this phenomenon.

- Sensitization in gas environments

In gas-phase services, sensitization has been widely documented as the root cause of intergranular degradation in austenitic stainless steels.

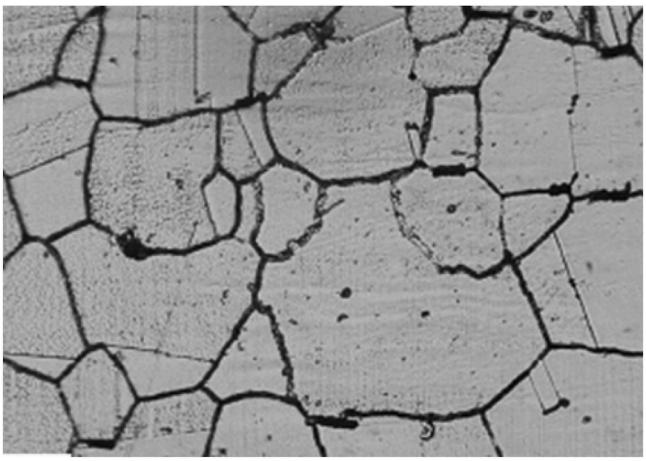

Fig. 8. Sensitized steel AISI 347 grain boundaries [91].

In the petrochemical industry, the overheating of AISI 347 furnace tubes at 512 °C in zones with coke deposition resulted in pit formation, as shown in Fig. 8, which acted as stress concentrators and triggered intergranular cracking [91]. Similar sensitization-induced cracking was later reported in AISI 347H boiler tubes after 3600 h of operation at 590 °C [92]. Even in unwelded 347H tubing, long-term exposure can promote failure: intergranular attack with pronounced ditching was identified after 25 years at relatively moderate service temperatures of 270–310 °C [93]. These cases emphasize that extended exposure to gas environments accelerates sensitization damage, irrespective of welding condition or the nominal operating range.

Beyond the 347-type steels, analogous phenomena have been reported for other grades. Bahrami et al. [94] showed that an AISI 304H elbow failed in a heat exchanger after 8 years at 400 °C, where intergranular embrittlement was exacerbated by internal oxidation. Comparative studies on AISI 310, 316L, and 347H revealed that after heat treatment in air at 480–720 °C, the pitting resistance of all alloys decreased at the highest temperatures owing to the precipitation of chromium carbide along the grain boundaries [95]. Interestingly, when 347 and 316 were directly compared, the higher carbon stabilization in 316 reduced susceptibility to intergranular brittle failure, whereas the lower carbon 347 alloys displayed enhanced vulnerability at 550–750 °C [96]. Thus, carbide stability and alloy carbon content are key differentiators of sensitization resistance in gaseous media.

In addition to sensitization-induced embrittlement, high-temperature gas exposure may promote mechanical softening of the material. For example, studies on 253 MA demonstrated stress softening under compression, with increasing strain rates (0.1 s^{-1} to 20 s^{-1}) leading to flow stress reduction, primarily due to deformation heating [97]. This indicates that, under service-like conditions, both sensitization and thermally activated flow instabilities can degrade the structural integrity of the austenitic steels.

- Sensitization in the solar salt environment

Sensitization in austenitic stainless steels exposed to molten salt environments pertinent to concentrated solar power (CSP) applications (approximately 500–600 °C) is predominantly linked to chromium depletion at grain boundaries, resulting from carbide precipitation in welded regions, particularly within the heat-affected zone (HAZ). Various mitigation strategies have been proposed for stabilized grades such as AISI 347H, including post-weld heat treatments [98,99], reduced heat input and interpass temperatures [100], and optimized welding techniques [101,102]. Nonetheless, the application of controlled stabilization treatments in large-scale molten salt storage tanks remains technically challenging. Comparative exposure of

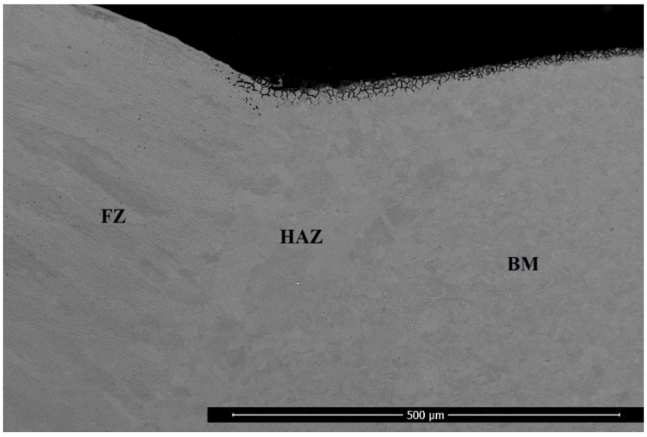

Fig. 9. Microstructure of 347H as-welded.

stabilized AISI 347 and non-stabilized AISI 316 at 600 °C revealed similar sensitized microstructures, with no immediate evidence of intergranular cracking within the investigated exposure times. This suggests that sensitization alone does not directly govern failure but serves as a precursor for stress- and environment-assisted degradation mechanisms [57].

- Stress Relaxation Cracking (SRC)

Stress Relaxation Cracking appears in the presence of a residual stress created by the welding process, particularly in the heat-affected zone (HAZ), where these stresses seem to be of high magnitude. Under high-temperature service conditions, residual stresses are not accommodated by plastic deformation owing to ductility exhaustion, resulting in intergranular cracking [103,104]. The different zones of a weld are characterized by distinct microstructural features. The fusion zone (FZ) presented a fully melted and resolidified structure with dendritic grains, and the heat-affected zone (HAZ) exhibited microstructural transformations owing to thermal exposure, including coarse-grained regions near the fusion line and fine-grained areas farther away. Finally, the base metal (BM) retains its original microstructure and mechanical properties. Fig. 9 illustrates the microstructural characteristics of an AISI 347H stainless-steel weld fabricated using the MIG process without the application of post-weld heat treatment. The figure emphasizes the microstructural heterogeneity observed in the fusion zone, heat-affected zone (HAZ), and base metal.

In a nuclear power plant, a reactor built with AISI 304H failed due to sensitization after welding; the failure mechanism was likely stress relaxation cracking after verifying that the yield strength at 560 °C (service temperature) was not exceeded [105]. The analysis of the welding impact on tubes used in coal-fired power plants showed that the high temperature of welding in steels such as AISI 304H and AISI 347H produced an enlargement of grains and dissolution of precipitates that increased SRC susceptibility [106]. Chemically stabilized stainless steels, such as 321H, are commonly used at high temperatures but are susceptible to intergranular cracking in the heat-affected zone (HAZ) after welding. Experimental studies have shown that controlling key parameters, such as minimizing heat input, selecting tougher filler metals (e.g., E16.8.2), reducing weld thickness and residual stresses, applying appropriate post-weld heat treatments, and limiting external loads, can significantly reduce or even eliminate the risk of SRC [107]. In a doctoral dissertation by Py-Renaudie [108], it was concluded, in agreement with Lee's statement, that SRC susceptibility in the CGHAZ region is mainly produced by grain size after analyzing the welded components of AISI 316L(N). Pickle T. et al. [109] demonstrated by simulation and testing the critical threshold stress for AISI 347H welded and assessed the filler material, determining that E347-16 FZ is more susceptible to SRC than 347H HAZ, and defined an optimum post-welding heat treatment to mitigate SRC.

Stress relaxation cracking (SRC) is notably underreported in the literature compared to stress corrosion cracking (SCC) or creep-related failures, despite its significance in large welded components operating at elevated temperatures. This underreporting is primarily due to the inherent challenges in identifying SRC as a distinct failure mechanism, as it frequently occurs in the absence of an external corrosive electrolyte, under low applied stress, and over extended service durations. Furthermore, SRC damage is typically localized within the heat-affected zone and may be misclassified as creep cracking or intergranular corrosion, particularly when post-service metallographic evidence is scarce. In industrial concentrated solar power (CSP) installations, complex thermal histories, multiple weld passes, and constrained geometries further complicate the differentiation of SRC from other time-dependent degradation processes. Consequently, the actual contribution of SRC to long-term damage in high-temperature welded structures is likely underestimated, underscoring the need for targeted experimental studies and enhanced diagnostic criteria.

2.2. Stress corrosion cracking (SCC)

Stress corrosion cracking comprises a two-stage process: crack initiation and propagation [110]. During initiation, an occluded corrosion cell develops, leading to localized acidification and chloride ion concentration, which weakens the material and facilitates crack formation [111]. Cracks can grow rapidly, often following intergranular paths due to the weakened grain boundaries, mainly in family planes {1 1 1}, especially if the steel has been sensitized [112]. The propagation is accelerated by localized corrosion and mechanical stress, ultimately leading to material failure [113]. As illustrated in Fig. 10, corrosion can

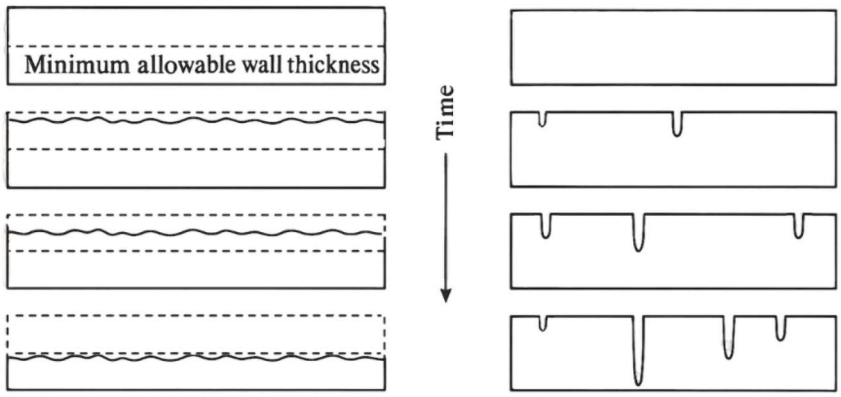

Fig. 10. Representation showing weakness due to corrosion.

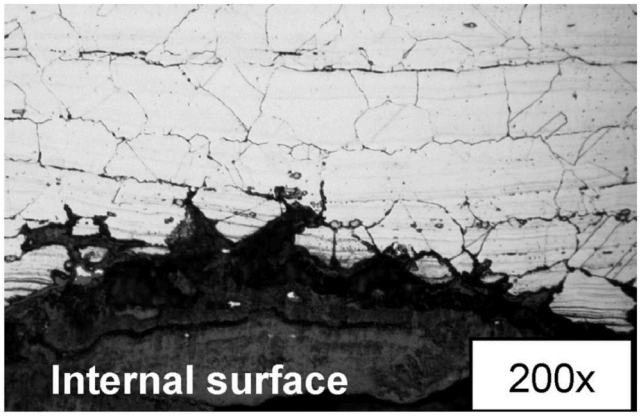

Fig. 11. Grain boundary attack results in corrosion and the dropping out of surface grains [116].

progressively reduce the effective wall thickness of the structural components. This loss of the load-bearing section leads to localized stress concentration, which, under sustained or residual stresses, facilitates the initiation and propagation of stress corrosion cracking.

Stress corrosion cracking (SCC) in austenitic stainless steels is a degradation mechanism that necessitates the concurrent presence of three factors: susceptible material condition, a specific corrosive environment, and tensile stress. The relative significance of each factor is highly contingent on the service environment, temperature, and alloy microstructure. Although the phenomenology of SCC may vary among aqueous, gaseous, and molten salt systems, the fundamental mechanisms are governed by environment-assisted crack initiation and propagation processes at the crack tip, frequently involving localized corrosion, film rupture, and hydrogen-related effects. Consequently, the following subsections examine the SCC behavior in diverse environments, emphasizing the predominant environmental drivers and their interactions with material conditions and stress.

2.2.1. *Stress corrosion cracking in aqueous and steam environments*

In aqueous and steam environments, chloride ions are significant factors in stress corrosion cracking (SCC). However, the generation and transport of hydrogen also play crucial roles, particularly at elevated temperatures. Under these conditions, hydrogen-assisted cracking can lead to either intergranular or transgranular SCC, depending on the degree of sensitization and the applied stress. Chloride ions (Cl^-) are consistently identified as key accelerators of stress corrosion cracking (SCC) in austenitic stainless steels. Chen et al. [114] reported that AISI 321 exposed to 300 °C aqueous solutions exhibited accelerated cracking in the presence of Cl^-. Similarly, crack growth studies on AISI 316Ti and AISI 316 L demonstrated that these alloys are unsuitable for piping at elevated temperatures when exposed to water containing 100 mg/L of chloride [115]. Industrial failures further confirm these findings: heater tubes made of AISI 321 in petrochemical plants failed between 130 and 345 °C because of Cl^- in crude oil, producing intergranular SCC, As illustrated in Fig. 11, attacks on grain boundaries can result in localized corrosion and the detachment of surface grains, thereby underscoring the vulnerability of austenitic stainless steels to intergranular degradation under high-temperature conditions [116].

Sensitization significantly heightens the susceptibility of austenitic stainless steels to stress corrosion cracking, particularly in welded components. Laboratory tests in boiling $MgCl_2$ demonstrated a strong correlation between the degree of sensitization and intergranular or transgranular cracking in AISI 304H and AISI 347, especially within the HAZ [117–119]. Optimized filler metal selection has been shown to mitigate stress-related cracking in stabilized grades [120]. Electrochemical studies provide additional insights into the SCC thresholds. Under reactor-relevant conditions, AISI 304 in the as-welded state was shown to be immune to intergranular SCC when exposed underwater at 274 °C for applied potentials below 0.4 V [121]. However, microstructural factors remain critical. The stress corrosion cracking susceptibility of AISI 316L welds was evaluated through long-term U-bend tests in a moderately aggressive electrolyte. Microcracks were initiated at pits within the heat-affected zone (HAZ), which is the region most affected by plastic deformation. Accelerated tests under constant current reproduced similar damage in shorter times, confirming the HAZ as the critical zone for SCC initiation [122]. Welding-induced sensitization in AISI 347 has been linked to solidification kinetics, where rapid cooling leads to gamma columnar dendrites with inter-dendritic segregation and intermetallic compounds; these features, along with porosity, strongly increase cracking susceptibility [123,124].

Taken together, these studies demonstrate that SCC in aqueous and steam environments is not governed by a single factor but rather by the synergistic effects of chloride concentration, sensitization degree, welding microstructure, and the electrochemical potential. Although filler metal optimization and careful control of welding parameters can reduce susceptibility, environmental chloride content, and post-welding sensitization, they remain persistent challenges in industrial services. Recent investigations into additively manufactured, precipitation-hardened austenitic stainless steel, produced via laser powder bed fusion, have revealed exceptional resistance to stress corrosion cracking (SCC) in high-temperature water at 325 °C. The alloy is characterized by equiaxed grains and nanoscale $TiAlNi_2$ precipitates located at cell boundaries, which serve to blunt SCC crack tips and enhance repassivation [125]. These results underscore the potential of microstructural design in mitigating SCC and provide a foundation for examining SCC behavior in more aggressive environments, such as molten salts, as discussed in the subsequent section.

2.2.2. *Stress corrosion cracking in molten salt environments*

In molten salt systems, SCC mechanisms differ from those in aqueous environments; however, mechanical strain remains decisive. Susceptibility to stress corrosion cracking (SCC) is significantly influenced by trace impurities, such as moisture and chloride ions. These impurities can destabilize protective oxide films and facilitate corrosion. The presence of H_2O in molten salts has been demonstrated to markedly increase SCC susceptibility by modifying the redox conditions and enhancing localized corrosion in stressed regions. Studies have consistently shown that a higher applied or residual strain reduces the time to crack initiation in austenitic stainless steels. For example, Prabha et al. [126] demonstrated that AISI 304H immersed in a boiling saturated magnesium chloride solution exhibited accelerated cracking under increased strain, confirming the strong stress dependence of SCC.

Within concentrated solar power (CSP) systems, the behavior of alloys in contact with molten salts provides further insight. A cold-worked alloy 601 immersed in a ternary eutectic carbonate mixture (32.1% Li_2CO_3 – 34.5% K_2CO_3 – 33.4%Na_2CO_3) at 450 °C showed evidence of sensitization followed by SCC, driven by oxidation-assisted processes [127]. Similarly, post-failure analysis of CSP receiver tubes made of 253 MA revealed that cyclic thermal stresses, combined with molten salt corrosion, produced intergranular cracking localized near welds [128].

These results suggest that while chloride-induced SCC dominates in aqueous systems, the interplay between strain, sensitization, and oxidation processes is more critical in molten salt environments. The susceptibility is further amplified by the operational realities in CSP receivers and tanks, such as thermal cycling and stress concentrators near the welds. Unlike aqueous environments, where the chloride content alone can drive SCC, molten salt cracking reflects a multifactorial mechanism in which the microstructure, strain state, and oxidation jointly determine the service life of the material.

2.3. *Creep*

Creep degradation in austenitic stainless steels is primarily

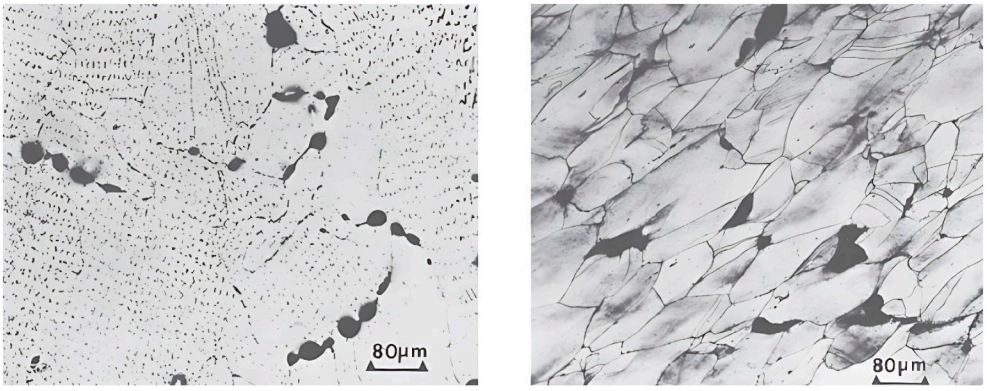

Fig. 12. Left: r-type voids in AISI 316L weld metal, right: w-type voids in AISI 316, after creep damage [131].

influenced by factors such as temperature, applied stress, microstructure, and service environment. In high-temperature energy systems, additional factors such as component geometry, welding-induced heterogeneities, and environmental interactions further affect the creep damage. This section is structured to initially summarize the fundamental mechanisms of creep, followed by an examination of their manifestation in several material conditions and specific service environments pertinent to high-temperature applications.

2.3.1. Creep mechanisms and controlling parameters

Creep rupture in austenitic stainless steels can exhibit either ductile or brittle behavior, depending on the deformation and damage mechanisms involved. Ductile fracture typically occurs through transgranular failure, whereas brittle rupture proceeds via the nucleation, growth, and coalescence of grain boundary cavities [129]. At elevated temperatures, the dominant mechanism often transitions toward intergranular processes, where microvoids form along grain boundaries and progressively link to form cracks.

The evolution of these cavities has been studied extensively. Early-stage voids, typically between 0.1 and 0.5 μm in diameter, can coalesce into macroscopic cracks several millimeters long under prolonged thermal exposure [130]. Two characteristic types of grain boundary cavities are commonly observed in intergranular creep: wedge-type voids (w-type), which initiate at triple junctions and promote intergranular crack propagation, and rounded or r-type voids, which appear as isolated microcavities along grain boundaries. Fig. 12 illustrates the characteristic types of cavities usually found in intergranular creep damage in austenitic steel, namely r-type and w-type cavities, which tend to form at grain boundary triple junctions. The formation and extent of these cavities provide a measure of the dominant creep mechanism, with r-type cavities being associated with diffusion-controlled mechanisms and w-type cavities with stress-assisted grain boundary sliding and crack formation. In CSP hot tanks, where the temperature is approximately 560 °C and creep loading is applied, the formation and growth of these cavities can be considered a precursor to intergranular fracture, particularly in weld areas [131].

Collectively, these observations indicate that the creep rupture behavior of austenitic steels results from the competition between transgranular deformation and intergranular damage mechanisms. The relative dominance of each mechanism depends on factors such as temperature, applied stress, alloy composition, and microstructural stability. Therefore, understanding the nucleation and evolution of cavities is crucial for predicting the long-term creep performance in high-temperature service environments.

The creep behavior of austenitic stainless steels is strongly influenced by the geometrical and microstructural factors that govern stress distribution, deformation mechanisms, and long-term stability. The thickness of the components can significantly alter the creep response. Tests conducted on HK40 stainless steel sheets of various thicknesses demonstrated that thicker sections are more prone to crack propagation, likely due to the transition from plane stress to plane strain conditions, which increases the constraint and promotes intergranular cracking [132]. Complementary analyses of HK40 using creep-fatigue interaction tests at 800, 900, and 1000 °C with symmetrical loading waveforms confirmed that the predictive models for life estimation can achieve good accuracy under cyclic high-temperature conditions [133].

When comparing the short-term creep performances of austenitic steels for services near 750 °C, AISI 347 demonstrated superior resistance at high-stress levels. This advantage is attributed to the interaction between mobile dislocations and fine precipitates formed during thermal exposure or in the early stages of creep, which act as effective barriers to dislocation motion [134]. However, under prolonged exposure, the microstructural evolution becomes more complex. Long-term creep tests on AISI 347H conducted in air at 700 °C and 800 °C revealed that an increased temperature modified the distribution of precipitates and promoted nitrogen uptake. Although the ductility decreased under these conditions, the overall creep strength remained relatively stable, confirming the robustness of the alloy for extended high-temperature applications [135].

2.3.2. Effect of material condition on creep behavior

The creep performance of welded components is often governed by complex interactions between metallurgical heterogeneity, residual stresses, and thermal gradients introduced during welding. In gas-cooled reactor applications, for example, as-welded AISI 312S tested at 650 °C exhibited creep lifetimes that were more accurately predicted when using a stress-modified ductility exhaustion approach combined with the R5 procedure, highlighting the importance of incorporating local ductility effects into life prediction models [136].

Microstructural degradation within the heat-affected zone (HAZ) plays a decisive role in determining creep rupture behavior. Observations in high-temperature piping systems have shown that creep damage initiates in the HAZ, where void nucleation and growth eventually lead to macroscopic cracking. These failures are exacerbated by thermal stresses and structural changes, such as carbide coarsening and grain boundary weakening, which accelerate the reduction in service life [137].

Sensitization also interacts with creep deformation at high temperatures by promoting grain boundary oxidation and carbide precipitation, which accelerate damage under long-term exposure. While coarse grain structures generally enhance creep life by reducing grain boundary sliding, they may simultaneously increase susceptibility to sensitization-related degradation [138]. Studies on AISI 310S at 800 °C indicate that creep damage can be closely coupled with corrosion and sensitization phenomena through carbide precipitation and grain boundary oxidation [139].

The presence of cavities is a key factor in the deterioration of dissimilar-welded joints. Studies involving Inconel 625 and AISI 304H

exposed to 600–700 °C for up to 3000 h revealed that cavity formation along dissimilar interfaces significantly reduces creep resistance, reflecting the detrimental influence of the mismatch in thermal expansion and diffusion behavior across the weld boundary [140,141]. Similar degradation mechanisms have been reported for modified AISI 310S welded joints tested at 600 °C, where creep-induced intergranular cracking was associated with the coarsening of $M_{23}C_6$ carbides, grain heterogeneity, and elemental segregation near grain boundaries [142].

Recent computational studies have advanced our understanding of these phenomena by incorporating residual stress fields into the creep damage models. These analyses revealed that creep cavity nucleation and growth are inherently localized and influenced by the non-uniform stress distribution typical of welded microstructures [143]. Innovative experimental techniques have been implemented to complement these modeling studies. Digital image correlation (DIC) systems have been successfully used to monitor the deformation of AISI 316H welded specimens during long-term high-temperature creep tests, achieving excellent agreement with conventional extensometry and enabling full-field strain mapping over extended periods [144].

2.3.3. Environmental effects on creep

- Creep in water/vapor environments

The creep performance of austenitic stainless steels in water and steam environments is strongly influenced by oxidation kinetics, precipitate stability, and the synergistic effects of corrosion and deformation. In heat exchanger applications, creep curves of AISI 347 at 750 °C have been established for multiple stress levels, providing essential baseline data for long-term design under high-pressure vapor exposure [145]. Further investigations on AISI 347H under supercritical water-cooled reactor conditions at 800 and 850 °C revealed that creep deformation is dominated by dislocation–precipitate interactions. Transmission electron microscopy confirmed that NbC precipitates aligned along slip directions retarded dislocation motion, thus improving creep resistance through a particle-strengthening mechanism [146].

In advanced ultra-supercritical (A-USC) thermal power plants, the Sanicro 25 alloy was evaluated under cyclic loading conditions at 700 °C and 36 MPa. These studies demonstrated that the dwell time (duration of load application) can either extend or shorten the component lifespan, depending on the applied stress level. This highlights the dual role of stress relaxation and oxidation-assisted damage in determining the long-term creep life [147,148].

However, corrosion-assisted creep degradation remains a critical issue in power generation environments. Superheater tubes fabricated from AISI 321 and exposed to 620–670 °C exhibited accelerated creep damage associated with high temperature corrosion. The presence of liquid corrosive agents, likely from condensate impurities or molten ash, was shown to intensify microstructural degradation and reduce creep life [149].

Long-term service studies have emphasized the role of environmental exposure. Ex-service AISI 316H components operated between 550 and 600 °C developed an oxidized surface and a carburized sublayer, indicating a combined oxidation–carburization mechanism [140]. Similarly, AISI 304H exposed to 31,000 h of superheated steam at 570 °C showed extensive precipitation of carbides, carbo-nitrides, and intermetallic phases, together with significant dislocation rearrangement. Despite these transformations, the mechanical integrity of the alloy remained above the minimum design requirements, suggesting that short-term degradation does not necessarily imply immediate failure [150,151].

Overall, a comparative analysis of these studies indicates that environmental factors, particularly oxidation, carburization, and corrosion, play a decisive role in modifying the creep mechanisms of stainless steels. Therefore, predictive models for creep in steam-containing systems must explicitly account for these coupled processes to ensure accurate life assessments in next-generation power plants.

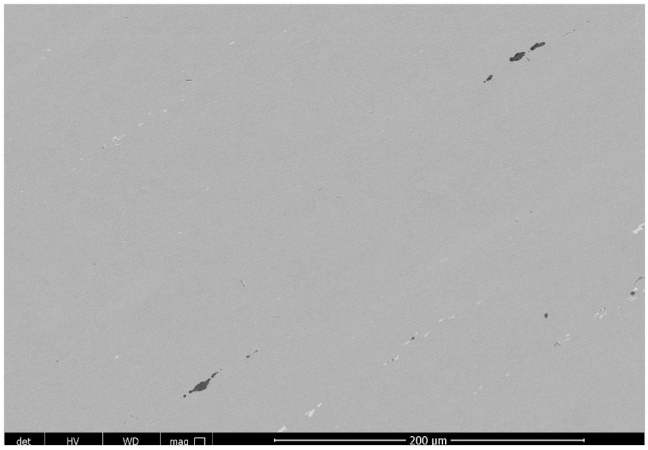

Fig. 13. Microcracks in 347H after creep test.

- Creep in molten salts applications

In molten salt storage systems, creep prevention is primarily achieved through careful design practices, specifically the selection of appropriate allowable stress limits following international standards, precise wall thickness calculations, and the evaluation of heat-affected zones (HAZ) under long-term creep conditions. Material selection is critical for concentrated solar power (CSP) plants that employ solar salt mixtures. Comparative testing between AISI 347H and AISI 316Ti at 570 °C in molten salt environments demonstrated superior corrosion and creep resistance for AISI 347H, in agreement with the design parameters and allowable stresses defined in ASME Section II-D [152]. Although most creep studies follow the ASTM E139 standard, this methodology does not explicitly account for specimens in direct contact with molten salts. Performing thermomechanical tests in such environments remains technically demanding because molten salts are highly corrosive and can cause leakage or degradation of the testing equipment. Consequently, only a few studies have attempted to replicate actual service conditions. For instance, Prieto et al. proposed an experimental setup to evaluate AISI 516 Gr70 exposed to solar salt at 380 °C for 168 h; the results indicated a reduction in the yield limit of the material, evidencing the impact of the corrosive environment on its mechanical integrity [153]. Fig. 13 presents the microcracking developed in AISI 347H after 600 h of exposure at an elevated temperature and indicates the early stages of damage accumulation before macroscopic failure. Microcracks, usually nucleating at grain boundaries or in regions influenced by surface conditions, show how cyclic thermal and mechanical loading can assist the processes of crack nucleation, even for relatively short exposure times. In CSP applications, such damage is particularly relevant within hot tanks and welded joints subjected to daily thermal cycling; under these conditions, the growth of microcracks can progressively interact with creep and corrosion mechanisms.

Another study at 565 °C with AISI 316L showed that the stainless steel exhibited a marked reduction in creep life in molten solar salt compared with air. Increasing stress shifted the cracking from intergranular to transgranular, whereas chloride impurities promoted intergranular cracking through substructure-assisted grain boundary corrosion. Creep deformation also accelerated corrosion by forming a fine-grained subsurface layer, although chlorides had a limited effect on the overall reduction in creep life [154].

In practical applications, creep life prediction for hot tanks in CSP plants is often performed using the ASME Section II-D guidelines in conjunction with Larson–Miller parameter-based equations. For austenitic alloys such as AISI 347H, the design stresses are

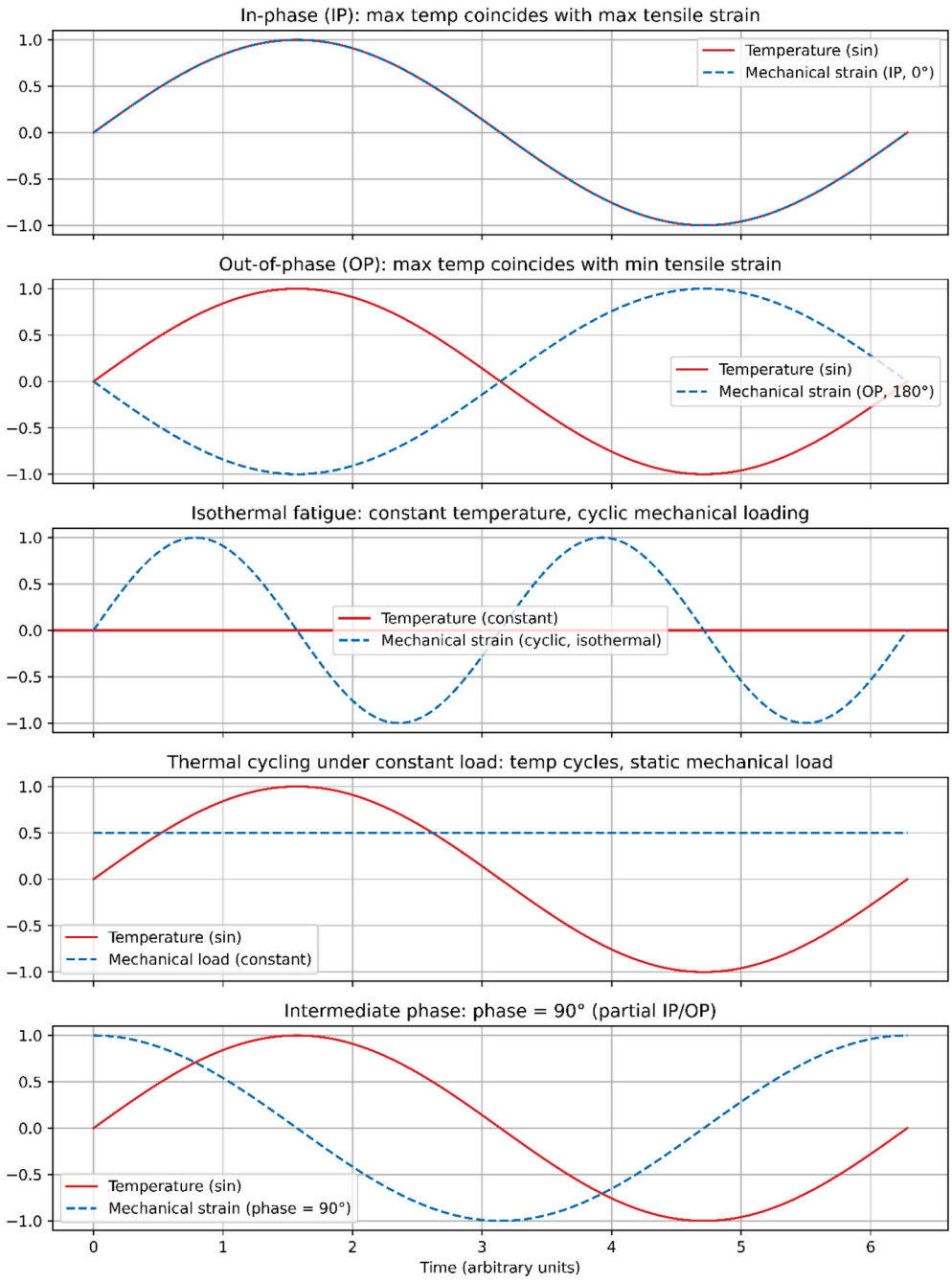

Fig. 14. Thermomechanical fatigue loading.

conservatively maintained below 100,000-h creep strength at operational temperatures, typically between 530 and 565 °C, to ensure long-term structural reliability.

2.3.4. *Implications for material selection and alternative alloys*

The pursuit of alternative materials with improved creep resistance for high-temperature applications has expanded beyond conventional austenitic stainless steels to include nickel-based superalloys. Among these, Sanicro 25 is a promising candidate. According to Chai and Forsberg [155], Sanicro 25 exhibits excellent long-term performance, achieving a predicted life of approximately 100,000 h at 100 MPa and 700 °C. Comparative studies against AISI 316H confirmed that Sanicro 25 demonstrates similar creep behavior while maintaining structural stability at higher temperatures, between 700 and 800 °C, during tests extending to 2000 h [156]. This improved thermal capability renders Sanicro 25 suitable for advanced ultra-supercritical (A-USC) power-generation systems.

However, even high-performance steels are susceptible to accelerated degradation under severe environmental conditions. Failures of reactor tubes used in styrene production have been attributed to combined overheating and carburization, where excessive oxidation at temperatures above 800 °C drastically reduces the component lifetime [157]. These findings highlight the need for environmental control to accompany alloy optimization to ensure reliable, long-term operation.

High-entropy alloys (HEAs) have been proposed as next-generation materials owing to their exceptional microstructural stability and solid solution strengthening. Nevertheless, after 23,500 h of testing at 600 °C, AISI 347H still outperformed the evaluated HEAs in terms of creep resistance, reaffirming the robustness of stabilized austenitic steels for long-duration service [158].

Another emerging family of steels, alumina-forming austenitic (AFA) steels, has been investigated for its potential to combine creep strength and superior oxidation resistance. Creep testing at 700 °C demonstrated that increasing the tungsten content enhanced precipitation hardening, thereby extending the creep life [159]. Additional studies have emphasized that a controlled balance between the aluminum and chromium concentrations is critical for forming a stable and protective alumina scale at high temperatures, without compromising mechanical integrity [160].

Surface engineering has also been explored to improve creep performance. Aluminized coatings followed by annealing have shown contrasting effects: while the presence of aluminum alone tends to degrade the creep life due to interfacial defects at the NiAl layer that reduce the effective load-bearing area, subsequent annealing mitigates these effects by promoting twin boundary formation and improving creep resistance [161].

In summary, although materials such as Sanicro 25, AFA steels, and HEAs offer promising pathways toward higher temperature capabilities, traditional Nb-stabilized austenitic grades, such as AISI 347H, continue to demonstrate competitive or superior creep performance. Future strategies will likely rely on hybrid approaches that combine alloy design, microstructural control, and optimized surface treatments to achieve sustainable performance under extreme thermal and environmental conditions.

2.4. Fatigue

Under dynamic mechanical loading, materials are subjected to cyclic plastic deformation, either localized or widespread, while a dislocation substructure progressively develops to accommodate the imposed strain. During this process, microcracks nucleate at the surface or within the bulk material and subsequently grow and coalesce until a final fracture occurs [162].

2.4.1. Fundamental fatigue mechanisms and regimes

The fatigue behavior of austenitic stainless steels is strongly influenced by temperature, grain size, and their microstructural stability. At elevated temperatures, coarse-grained austenitic alloys have been observed to exhibit internal fracture mechanisms in the high-cycle fatigue regime, where damage accumulates primarily through dislocation interactions and internal crack propagation rather than surface initiation [163].

Welded joints are particularly vulnerable because of their heterogeneous microstructures. The heat-affected zone (HAZ) of weldments often undergoes local thermal cycling, resulting in grain coarsening and carbide precipitation, both of which promote fatigue crack initiation. For instance, pipes manufactured from AISI 347H stainless steel failed under thermal stress fatigue owing to the microstructural alterations produced during welding, highlighting the detrimental influence of HAZ transformations on the cyclic durability [164].

2.4.2. Effect of loading mode: mechanical, thermal and thermo-mechanical fatigue

In nuclear and energy-generation systems, components such as tubes and pipes are often subjected to simultaneous thermal and mechanical loads, making accurate fatigue life predictions essential for safe operation of these components. Consequently, several studies have developed models that incorporate both thermal and mechanical fatigue effects in controlled-air environments.

- Thermo-mechanical fatigue

Thermo-mechanical fatigue (TMF) combines cyclic temperature and mechanical loading, and the relative phase between the two cycles strongly controls the damage mechanisms. In-phase (IP) TMF (max temperature coincident with max tensile strain) enhances oxidation/creep-assisted damage, whereas out-of-phase (OP) TMF (max temperature coincident with minimum tensile strain) emphasizes cyclic plasticity and mismatch strain. Isothermal fatigue maintains a constant temperature while mechanical load cycles are applied, isolating purely mechanical fatigue. A different, practically relevant case is thermal cycling under a constant load, where the temperature oscillates but an approximately static stress is applied; this promotes thermal-strain mismatch and stress relaxation and can drive thermal-fatigue mechanisms. Partial phase angles (e.g., 90°) produce intermediate behavior and are useful to map transition between IP and OP [165,166]. In Fig. 14, a description of different loading conditions in thermo-mechanical fatigue, such as in-phase, out-of-phase, and isothermal, is graphically depicted and it is of high relevance to CSP systems. In in-phase loading, where the maximum stress and maximum temperature occur simultaneously, accelerated degradation, owing to the joint action of reduced material strength and increased mechanical loads, can usually be observed. In contrast, even in out-of-phase loading, there may be favorable mechanisms of crack initiation related to temperature gradients. Such loading conditions aptly describe the operating conditions in molten salt tanks and pipelines, where thermal and mechanical loadings related to the start-up and shutdown procedures cannot be simulated in isothermal fatigue tests. Ramesh et al. [167] conducted a comparative study of AISI 347 and AISI 316L stainless steels under thermomechanical fatigue, combining temperature variations between 100 and 340 °C with different mechanical strain amplitudes ($\Delta\varepsilon\_mech/2 = 0.3\%$ and 0.5%). Three distinct testing configurations were employed: *in-phase* (maximum strain coinciding with the maximum temperature), *out-of-phase* (maximum strain coinciding with the minimum temperature), and *isothermal fatigue* tests (constant temperature). These results indicate that both isothermal and out-of-phase conditions significantly reduce the fatigue life, whereas AISI 316L consistently exhibits a longer lifetime than AISI 347 under all conditions [168].

Taira S [169]. further investigated the response of AISI 347 under thermal cycling combined with alternating mechanical stress at a mean temperature of 400 °C in air. This study emphasizes the critical influence of strain amplitude on fatigue behavior at elevated temperatures, revealing that mechanical and thermal fatigue are closely interrelated through the plastic strain component that governs cyclic deformation.

The thermomechanical fatigue behavior of Sanicro 25 was comprehensively characterized in the temperature range of 250–700 °C. This research explored crack initiation and propagation mechanisms, cyclic hardening and softening responses, and established fatigue life curves, providing a detailed understanding of its performance under high-temperature cyclic loading [170].

- Low-cycle and high-cycle fatigue

The fatigue behavior of austenitic stainless steels is highly influenced by their chemical composition, temperature, and cyclic deformation mechanisms. For AISI 347, studies performed at 300 °C under Low Cycle Fatigue (LCF, <1000 cycles), High Cycle Fatigue (HCF), and Very High Cycle Fatigue (VHCF) regimes revealed that metastability plays a significant role in the fatigue lifetime. During cyclic loading, various deformation mechanisms, such as planar or wavy slip, stacking fault formation, and mechanical twinning, are activated alongside transformation processes ($\gamma \rightarrow \varepsilon$, $\gamma \rightarrow \varepsilon \rightarrow \alpha'$, $\gamma \rightarrow \alpha'$), each contributing differently to the overall fatigue response [162].

LCF testing has also been applied to assess the fatigue resistance and predict the lifetime of welded AISI 304H specimens at 750 °C under tensile loading conditions. The results highlighted the critical influence of fatigue parameters, such as load amplitude, on the differences in the failure mechanisms between the base and weld metals. These findings highlight the necessity of incorporating both material and microstructural effects into fatigue life predictions [171].

Further investigations on AISI 316H at 550 °C demonstrated brittle

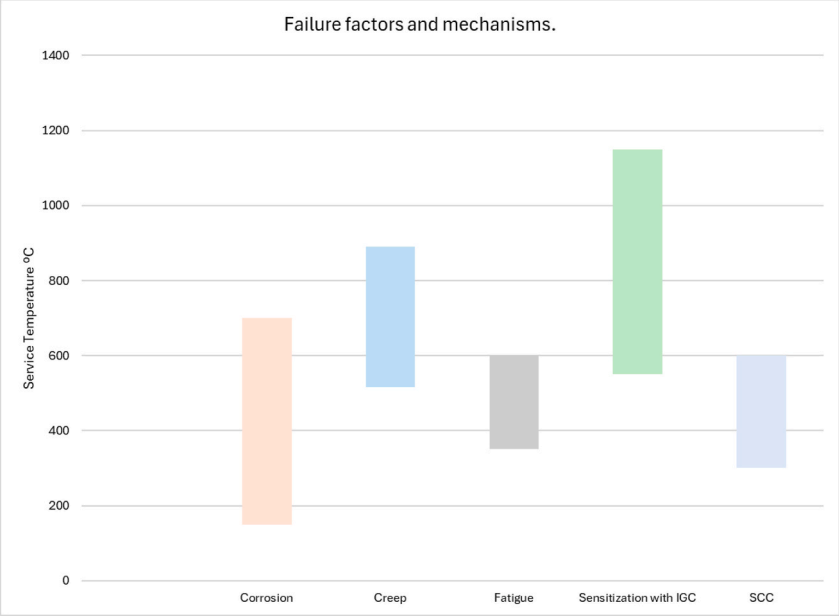

Fig. 15. Summary of the dominant failure mode as a function of temperature for the studied austenitic stainless steels.

transgranular fractures during the LCF testing. The number of crack initiation sites increased with the strain amplitude, and the material exhibited non-Masing behavior at low strain amplitudes (0.2%–0.6%) but transitioned to Masing behavior at higher strain levels, which was attributed to the evolving dislocation configurations during cyclic loading [172,173].

Similarly, fatigue analyses of AISI 321 stainless steel revealed that the dependence of fatigue life on strain rate arises primarily from a shift in the dominant fracture mode from transgranular to intergranular cracking as the cyclic deformation progresses [174].

2.4.3. *Environmental effects on fatigue*

- Fatigue in water/vapor environments

The fatigue behavior of components in water and vapor environments is particularly important for components operating under cyclic thermal and mechanical loads, such as those in nuclear and power generation systems. Comparative assessments of austenitic stainless steels have revealed notable differences in their performance, depending on the alloy composition and microstructural characteristics.

For instance, AISI 316 N exhibited superior fatigue behavior compared to AISI 347 N at 330 °C under conditions representative of nuclear power plant applications. The longer fatigue life observed for AISI 316 N was attributed to differences in precipitate morphology; in AISI 347 N, niobium carbo-nitride precipitates exhibited a bimodal size distribution, which promoted localized stress concentrations and accelerated fatigue crack initiation [175].

An inelastic material model was also developed for AISI 316H to evaluate its suitability as a high-temperature reactor component. The model identified key parameters governing inelastic deformation over a range of temperatures but highlighted inconsistencies between 500 and 550 °C, which were attributed to dynamic strain aging (DSA) effects that altered the cyclic hardening behavior and fatigue resistance [176].

In another study, the failure of a gas generator plate fabricated from AISI 310S revealed fatigue cracking under a considerable temperature gradient. Microstructural analysis revealed sigma-phase precipitation, which induced local hardening and embrittlement, ultimately facilitating crack initiation and propagation under cyclic thermal stress [177].

- Fatigue in CSP components

Thermal fatigue is relevant to tank design because of routine start-up and shutdown operations. Cyclic thermal-mechanical stress design, following ASME Section VIII Div. 2 requirements and ASTM E606 low-cycle fatigue testing. The tank configuration, supports, and thermal gradients were designed to reduce stress concentrations.

In CSP molten salt storage tanks operating around 560 °C, material degradation is governed not by isolated mechanisms but by the interaction of cyclic thermal loads and sustained or residual mechanical stresses. Daily thermal cycling, start-up and shut-down operations, and temperature gradients across large welded structures generate complex thermo-mechanical stress states, particularly at the tank floor and welded joints. Under these conditions, creep deformation, stress relaxation cracking (SRC), and fatigue damage may act synergistically rather than independently [178].

Thermal cycling promotes strain accumulation and microstructural instability, while sustained stresses and residual welding stresses facilitate creep and stress relaxation processes. This interaction accelerates crack initiation and propagation, especially in sensitized heat-affected zones, where grain boundary weakening, oxidation, and carbide precipitation coexist. Consequently, creep–fatigue interaction and SRC have emerged as dominant failure modes in CSP hot tanks, highlighting the limitations of conventional design approaches that treat creep, fatigue, and corrosion separately [179].

2.4.4. *Factors affecting fatigue resistance*

Thermal cycling experiments have shown that the holding temperature can reproduce creep-like mechanisms, significantly influencing the fatigue behavior. In AISI 309 stainless steel tested between 100 °C and 900 °C, microvoid coalescence and cavity formation at the grain and twin boundaries were observed, promoting crack initiation and propagation [180].

Comparative studies on AISI 316, AISI 316 N, and Sandvik 253 MA have examined the effects of nitrogen content on the low-cycle fatigue resistance. The addition of nitrogen was found to restrict the cross-slip of dislocations and promote planar slip, thereby enhancing the fatigue strength [181]. Another comparison between AISI 316 and 253 MA revealed that AISI 316 exhibited higher fatigue resistance at 750 °C; however, at 900 °C, 253 MA outperformed AISI 316 because of the

influence of the hold time at maximum strain, which favors stress relaxation and improves the cyclic life [182].

Surface modification has also been investigated to enhance the fatigue resistance of austenitic steels. For AISI 347, cryogenic turning improved the fatigue life and reduced the plastic strain amplitude through specific surface morphology changes [168]. In the case of AISI 330 wire exposed to carburizing and oxidizing environments, post-failure analysis revealed the transformation of silicide phases (H, G, NbC) into the G-phase, along with the formation of carbides that contributed to surface damage and eventual fracture [183].

Cast austenitic HK40 alloys have been extensively studied to evaluate the effects of tungsten content on their mechanical and fatigue properties. The results indicate that increasing the tungsten content improves the strength but reduces the ductility, with an optimal content of approximately 2 wt% for low-cycle fatigue performance [184]. Additional LCF studies on HK40 demonstrated improved fatigue resistance at elevated temperatures under large stress amplitudes [185]. Long-term service assessments of HK40 tubes after 21 years of operation employed the Z-parameter method to estimate the accumulated damage, residual life, and degradation of the rupture properties, effectively linking the confidence levels to the damage progression over time [186].

In the automotive sector, comparative evaluations of steels for exhaust manifold applications have identified ferritic steels as cost-effective alternatives to traditional austenitic steel grades. These ferritic steels exhibit excellent creep and fatigue resistance at temperatures of up to 1000 °C, making them promising options for high-temperature cyclic services [187].

Despite the acknowledged significance of thermal and thermo-mechanical fatigue in high-temperature components, experimental data concerning these mechanisms within molten-salt environments remain exceedingly limited. This constraint is primarily attributed to the absence of specialized testing facilities capable of concurrently applying controlled cyclic mechanical loads and thermal gradients while safely containing the highly corrosive molten salts. Consequently, most of the fatigue data available for austenitic steels have been generated in air or aqueous environments, necessitating cautious extrapolation to Concentrated Solar Power (CSP) molten salt systems. Nonetheless, in CSP hot tanks and piping systems, repeated start-up and shutdown operations, load following, and temperature stratification during charge–discharge cycles impose cyclic thermal stresses that may synergistically interact with corrosion processes. Even in the absence of direct experimental fatigue data for molten salts, these combined effects are anticipated to play a critical role in crack initiation, damage accumulation, and life prediction under highly corrosive high-temperature service conditions.

Fig. 15 summarizes the findings of the studies described above and underscores the importance of temperature as the dominant failure factor, enabling targeted inspection and prevention strategies based on operating conditions.

- Above 300 °C: Failures are dominated by SCC, especially in stainless steels. Additionally, corrosion is frequent in cooler or condensing regions, where the protective oxide layers are compromised.
- Around 400 °C: At this temperature, the damage mechanisms are primarily related to thermal fatigue and mechanical fatigue, often arising from thermal cycling and stress concentration points. In some cases, localized oxidation can coexist with fatigue, accelerating material degradation through surface embrittlement.
- Above 400 °C: The most common mechanisms are general corrosion, mainly due to sustained high-temperature oxidation, sensitization, IGC, and creep, especially in components exposed to prolonged thermal stress. These processes can significantly affect the long-term mechanical integrity of high-temperature components.

Fig. 15 illustrates the activation temperature ranges of the predominant degradation mechanisms under generic high-temperature conditions. In contrast, within aggressive molten salt chemistries, such as fluoride and chloride salts, corrosion emerges as the primary failure mechanism above approximately 500 °C, frequently accelerating or obscuring other mechanisms, such as creep, fatigue, or stress corrosion cracking (SCC).

3. Design implications and mitigation strategies for CSP molten salt tanks CSP

From the above, reviewed failure mechanisms, some strategies can be deduced regarding the application of austenitic stainless steels at a working temperature of approximately 560 °C in high-temperature CSP molten-salt storage tanks.

Although the current ASME and API design codes offer comprehensive guidelines for mechanical integrity and permissible stress levels, they do not explicitly address long-term degradation mechanisms associated with molten salt chemistry, impurity accumulation, or thermal cycling. Therefore, mitigation strategies such as welding optimization, material stabilization, and salt chemistry control are crucial supplements to code-based design for CSP hot tanks.

3.1. Material selection and alloy design

In conventional austenitic stainless steel families, stabilized grades of steel, such as AISI 347H, have been found to resist the degradation of both creep and corrosion more efficiently than non-stabilized counterparts, such as AISI 316L, particularly in the presence of liquid molten nitrate salt environments for longer periods of time. Additionally, the presence of Nb in the composition aids in the precipitation of stable NbC, thereby increasing the resistance to creep. A disadvantage of the stabilization process is that it is not solely capable of resisting sensitization and intergranular attack at higher temperatures, particularly in welded areas. Nickel-based alloys, such as Inconel 625, perform better in corrosive environments, particularly in molten salt environments; however, they can experience accelerated degradation in environments containing chlorides, and their use is economically prohibitive at the tank scale [188].Recent investigations into high-temperature steam environments have revealed that the integrity of oxide layers is predominantly influenced by the residual stress and strain gradients within multilayer oxide scales. Notably, ultrasonic surface rolling processing (USRP) has been shown to markedly enhance the fracture resistance of Fe_3O_4/Cr_2O_3 oxide systems by diminishing tensile stress gradients, fostering compressive interfacial bonding, and alleviating strain incompatibility at the oxide–metal interfaces. Although these studies were conducted in steam, the findings offer pertinent mechanistic insights for concentrating solar power (CSP) molten salt systems, where brittle oxide cracking and interfacial decohesion can similarly expedite corrosion-assisted damage under thermal and mechanical load conditions [189].

3.2. Welding, fabrication, and post-weld treatments

Welded joints remain a damage-sensitive location in CSP storage tanks. Factors such as multiple passes, thick plates, and restrained geometries contribute to high residual stresses and a coarse-grained heat-affected zone, making it prone to stress relaxation cracking or intergranular creep cracking failures. Its prevention measures entail using low heat inputs during the process, controlling interpass temperatures, or performing adequate post-welding heat treatments to relieve residual stresses, which may suppress the efficiency of stress stabilization. The stabilization of stresses at the base of a storage tank or at a junction of a tank also merits attention, where a tank may be prone to combined failures owing to its operation or corrosion effects [190].

3.3. Surface protection and environmental control

Surface modification methods, such as aluminide coating and diffusion-based protection layers, show promise for suppressing the corrosion rates in molten salt environments. However, these coating methods are prone to degradation during thermal cycles and creep deformations. It is also necessary that salt chemistry, especially chloride ion content, water, and redox states, are properly managed at the surface [191].

3.4. Multiscale and computational approaches

Recent reviews of molecular dynamics (MD) modeling of molten salts have highlighted the potential of atomistic simulations to augment experimental investigations in concentrated solar power (CSP) applications. MD analyses have demonstrated that the chemical composition of salts significantly influences their transport and thermophysical properties, while also providing a framework for examining corrosion-related phenomena at the interface level. Notably, large-scale and long-duration simulations enhanced by machine learning techniques have been proposed as a promising approach to investigate the corrosion mechanisms and the evolution of properties in molten salts, thereby addressing the limitations of experimental methods in long-term and large-component testing [192].

3.5. Emerging alloys and future research directions

Existing high-temperature materials, such as alumina-forming austenitic (AFA) steels and specific high-entropy alloys (HEAs), have been identified as candidates for next-generation concentrated solar power (CSP) systems operating at temperatures above 600 °C. Although these materials showed good oxidation resistance and several samples even showed satisfactory resistance against creep in qualification testing, their suitability when exposed to molten nitrate or chloride salts for long-term exposure, their joinability, and the cost-benefit ratio still require analysis. Future analyses should focus on comprehensive testing with respect to corrosion, creep, and fatigue performance at the operational conditions of a CSP plant, as well as the modeling of these materials at operational conditions.

4. Conclusions and future work

This review has examined the performance of austenitic stainless steels under high-temperature service conditions, including in the application for concentrated solar power (CSP) systems. A wide range of austenitic grades, including stabilized and low-carbon grades, has been examined for mechanical and chemical stability at high temperatures. Corrosion mechanisms, particularly oxidation and carburization, are established, and several protective strategies have been proposed in the literature.

In addition, mechanical degradation modes such as creep, thermal fatigue, and stress relaxation cracking (SRC) have been studied in specific high-temperature environments. However, despite the progress in characterizing the mechanisms, experimental studies involving exposure to molten salt are limited. With the growing application of molten salts as heat transfer and storage fluids in CSP, this is a significant deficiency in the current state of knowledge.

In order to enhance the performance and reliability of CSP systems at high temperature, the following recommendations are proposed:

- Enhance experimental work in molten salts: While corrosion in oxidizing conditions is well established, the behavior of austenitic steels in molten salt conditions—especially under mechanical stress—needs to be investigated further. This includes studies on long-term degradation, pitting, and localized corrosion mechanisms under static and dynamic salt exposure.
- Implement mechanical testing in service-like conditions: Mechanical properties such as creep resistance, fatigue life, and stress relaxation susceptibility to cracking should be tested in molten salt environments at the operating temperatures (typically 500–600 °C). Thermo-mechanical and corrosion combined testing will give a more realistic indication of the performance of the material.
- Compare stabilized and non-stabilized austenitic grades: Alloys such as AISI 347H (Nb-stabilized) and AISI 316L (low-carbon) exhibit varying mechanisms of stabilization against intergranular attack and sensitization. Further comparative work is needed to clarify how these variations influence long-term behavior in CSP environments.
- Standardize test procedure and reporting: Creating consistent means of corrosion and mechanical testing in molten salts will improve the comparability of data among research. Using international standards where feasible and modifying them for service in molten salts, would benefit the field.

Table 4
Key comparative findings and design implications for CSP applications.

Failure mode	Dominant material	CSP relevance	Key driver	Mitigation
Creep	347H	High	Temperature + time	Nb stabilization
SRC	347H (welds)	Very high	Residual stress	PWHT, weld control
SCC	316L	Moderate	Cl^- + stress	Salt control
Fatigue	All	High	Thermal cycling	Design flexibility

Monitoring weld and fabrication influence: Since the welded joints are likely to be one of the vulnerabilities, research would also include testing of SRC as well as corrosion in the fusion lines and HAZ under CSP conditions.

The comparative analysis presented in Table 4 indicates that the selection of materials for CSP hot tanks should not be based solely on corrosion resistance. Instead, failure mechanisms such as stress relaxation cracking, creep, and thermomechanical fatigue, significantly influenced by welding practices and thermal cycling, are predominant at operating temperatures around 560 °C. Stabilized austenitic steels, such as AISI 347H, offer enhanced resistance to these interconnected degradation processes, thereby supporting their continued application in large-scale molten salt storage systems.

Declaration of competing interest

The authors declare the following financial interests/personal relationships which may be considered as potential competing interests: Fernandez, A.I. reports financial support was provided by Spain Ministry of Science Innovation and Universities. Fernandez, A.I. reports financial support was provided by European Union. Fernandez, A.I. reports financial support was provided by Government of Catalonia Agency for Administration of University and Research Grants. Fernandez, A.I. reports financial support was provided by Government of Catalonia. Prieto, C. reports financial support was provided by Spain Ministry of Science Innovation and Universities. Prieto, C. reports financial support was provided by European Union. Osorio, J.D. reports financial support was provided by Alliance for Sustainable Energy LLC. Osorio, J.D. reports financial support was provided by Solar Energy Technologies Office. If there are other authors, they declare that they have no known competing financial interests or personal relationships that could have appeared to influence the work reported in this paper.

Acknowledgements

The authors would like to thank the Grant PID2021-123511OB-C31, PID2021-123511OB-C32 and Grant RED2024-153629-T funded by

MCIU/AEI/10.13039/501100011033 and by FEDER, UE, and the Grant TED2021-132216A-I00 European Union by Next Generation EU/PRTR. This work was authored in part by the National Renewable Energy Laboratory, operated by Alliance for Sustainable Energy, LLC, for the U. S. Department of Energy (DOE) under Contract No. DE-AC36-08GO28308. Partial support was provided by the U.S. DOE – Solar Energy Technologies Office (SETO) under the agreement 52729 – "Addressing Failures in Molten Nitrate Thermal Energy Storage Tanks Through the Design and Fabrication Optimization of the Tank Floor and Experimental Validation." The views expressed in the article do not necessarily represent the views of the U.S. DOE or the U.S. Government.

Prof. Fernández thanks the Catalan Government for the quality accreditation and funding given to their research group DIOPMA (2021 SGR 00708). DIOPMA is a certified agent TECNIO in the category of technology developers from the Government of Catalonia.

References

[1] Philibert C, et al. Technology roadmap: solar thermal electricity. 2014. Paris, France.
[2] Calderón A, Barreneche C, Prieto C, Segarra M, Fernández AI. Concentrating solar power technologies: a bibliometric study of past, present and future trends in concentrating solar power research. Frontiers Media S.A; Jun. 18, 2021. https://doi.org/10.3389/fmech.2021.682592.
[3] Cozzi L, et al. World energy outlook 2020. 2019.
[4] Prieto C, Tagle-Salazar PD, Patiño D, Schallenberg-Rodriguez J, Lyons P, Cabeza LF. Use of molten salts tanks for seasonal thermal energy storage for high penetration of renewable energies in the grid. J Energy Storage May 2024;86. https://doi.org/10.1016/j.est.2024.111203.
[5] Osorio JD, et al. Failure analysis for molten salt thermal energy storage tanks for In-Service CSP plants. 2024 [Online]. Available: www.nrel.gov/publications.
[6] Guo H, et al. Analysis of thermal and mechanical properties with inventory level of the molten salt storage tank in central receiver concentrating solar power plants. Appl Therm Eng 2025;260(Feb). https://doi.org/10.1016/j.applthermaleng.2024.124984.
[7] Khatak H, Raj B. Corrosion of austenitic stainless steels mechanism, mitigation and monitoring. Woodhead publishing; 2002.
[8] Smallman RE, Ray J, Bishop. Metals and materials : science, processes, applications. Butterworth-Heinemann; 1995.
[9] Bhadeshia HKDH, Honeycombe RWK. Steels: microstructure and properties. third ed. Butterworth-Heinemann; 2017.
[10] Thomas RD. HAZ cracking in thick sections of austenitic stainless steels. II. Weld J 1984;63(12):355s–68s.
[11] Dhooge A. Survey on reheat cracking in austenitic stainless steels and Ni base alloys. Weld World 1998:206–19.
[12] Cullen TM, Freeman JW. Metallurgical factors influencing hot ductility of austenitic steel piping at weld heat-affected zone temperatures [Online]. Available: http://www.asme.org/about-asme/terms-of-use; 1963.
[13] Lai GY. High-temperature corrosion and materials applications. ASM international; 2007.
[14] Ningshen S, Mudali UK. Uniform corrosion of austenitic stainless steels. In: Corrosion of austenitic stainless steels. Elsevier; 2002. p. 37–73. https://doi.org/10.1533/9780857094018.74.
[15] Raj B, Kalyanasundaram P, Dewangan SK. Corrosion detection and monitoring in austenitic stainless steels using nondestructive testing and evaluation techniques. In: Corrosion of austenitic stainless steels. Elsevier; 2002. p. 287–313. https://doi.org/10.1533/9780857094018.314.
[16] Russell B, Ham RK, Silcock JM, Willoughby G. Creep mechanisms in niobium-stabilized austenitic steels. Metal Science Journal Jan. 1968;2(1):201–9. https://doi.org/10.1179/030634568790443242.
[17] McEvily Arthur J. Metal failures mechanisms, analysis, prevention. second ed. Wiley; 2013.
[18] Fontana Mars G. Corrosion engineering. third ed. McGraw-Hill; 1986.
[19] Lister DH, Davidson RD, Mcalpine E. The mechanism and kinetics of corrosion product release from stainless steel in lithiated high temperature water. Corros Sci 1987;27(2):113–1411.
[20] Guttmann V, Marriott JB. The effects of corrosive atmospheres on time dependent mechanical properties. 1980.
[21] Kofstad P. Basic oxidation principles: growth of continuous scales. In: In surface engineering: surface modification of materials; 1983. p. 370–89.
[22] Yushandiana F, Setiana H, Pujiyulianto E. Case study: the failure analysis of pipe ASTM A351 HK-40 in reaction plant unit. J Fail Anal Prev Jun. 2020;20(3):663–70. https://doi.org/10.1007/s11668-020-00885-y.
[23] Gleeson B. Alloy degradation under oxidizing-sulfidizing conditions at elevated temperatures 61. Mater Res 2004;7(1):61–9.
[24] Shao MZ, Cui LS, Zheng YJ, Wang YX, Xing LL. Oxidation behavior of alloy HK40 in H2-H2O atmosphere. Mater Corros Sep. 2013;64(9):777–82. https://doi.org/10.1002/maco.201106336.
[25] Caceres-Valencia PG, Baiges IJ. Effect of elemental redistribution on the failure of centrifugally cast HK40 alloy. Apr. 2006. https://doi.org/10.1361/154770206X99334.
[26] Kaya AA, Krauklis P, Young DJ. Microstructure of HK40 alloy after high temperature service in oxidizing/carburizing environment I. Oxidation phenomena and propagation of a crack. Mater Char 2002;49:11–21.
[27] Walmsley JC, Albertsen JZ, Friis J, Mathiesen RH. The evolution and oxidation of carbides in an alloy 601 exposed to long term high temperature corrosion conditions. Corros Sci Dec. 2010;52(12):4001–10. https://doi.org/10.1016/j.corsci.2010.08.015.
[28] Jegede A, Vasantasree V, Hocking MG. Corrosion behaviour of HR-160 and HA-188 in a simulated waste incineration environment at 750 °C. J Mater Sci Lett 1995;14:858–60.
[29] Was GS, Teysseyre S, Jiao Z. Corrosion of austenitic alloys in supercritical water. Corrosion 2006;62:989–1005.
[30] Zhu Z, Xu H, Khan HI, Jiang D, Zhang N. Effect of exposure temperature on oxidation of austenitic steel HR3C in supercritical water. Oxid Metals Feb. 2019;91(1–2):77–93. https://doi.org/10.1007/s11085-018-9879-9.
[31] Shen Z, et al. Microstructure understanding of high Cr-Ni austenitic steel corrosion in high-temperature steam. Acta Mater 2022;226(Mar). https://doi.org/10.1016/j.actamat.2022.117634.
[32] Wang K, Wang J, Hu W. Evaluation of temperature effect on the corrosion process of 304 stainless steel in high temperature water with electrochemical noise. Mater Des Oct. 2015;82:155–63. https://doi.org/10.1016/j.matdes.2015.05.044.
[33] Yuan J, Wang W, Zhang H, Zhu L, Zhu S, Wang F. Investigation into the failure mechanism of chromia scale thermally grown on austenitic steel in pure steam. Corros Sci 2016;109:34–42.
[34] Nezakat M, Akhiani H, Penttilä S, Sabet SM, Szpunar J. Effect of thermo-mechanical processing on oxidation of austenitic stainless steel 316L in supercritical water. Corros Sci 2015;94:197–206.
[35] Klymenko AV, et al. Corrosion resistance of AISI 310s stainless steel in lead melt at a temperature of 450°C. Mater Sci Mar. 2023;58(5):591–6. https://doi.org/10.1007/s11003-023-00703-4.
[36] Zhao J, et al. High-temperature corrosion behavior of 316 H stainless steel in lead-bismuth eutectic containing cesium. Corros Sci 2024;236(Aug). https://doi.org/10.1016/j.corsci.2024.112282.
[37] Pan J, Leygraf C, Otsuka T, Jargelius-Pettersson RFA, Ivarsson B, Linden J. EIS study of high-temperature oxide films on a stainless steel (253MA)- influence of alloying elements. Mater Sci Forum 1998;289–292(PART 2):1181–92.
[38] Pour-Ali S, Weiser M, Truong Nguyen N, Kiani-Rashid AR, Babakhani A, Virtanen S. High temperature oxidation behaviour of AISI 321 stainless steel with an ultrafine-grained surface at 800 °C in Ar–20 vol.% O2. Corros Sci 2020;163(Feb). https://doi.org/10.1016/j.corsci.2019.108282.
[39] Dudziak T, Rząd E, Golański G, Solecka M, Boroń Ł, Wieczorek P. Paper: effect of aging process on steam oxidation behaviour of austenitic steels super 304H and HR3C. Int J Pres Ves Pip 2021;191(Jun). https://doi.org/10.1016/j.ijpvp.2021.104344.
[40] Cissé S, Laffont L, Tanguy B, Lafont MC, Andrieu E. Effect of surface preparation on the corrosion of austenitic stainless steel 304L in high temperature steam and simulated PWR primary water. Corros Sci Mar. 2012;56:209–16. https://doi.org/10.1016/j.corsci.2011.12.007.
[41] Rosser JC, et al. Steam oxidation of super 304H and shot-peened super 304H. Mater A T High Temp Jun. 2012;29(2):95–106. https://doi.org/10.3184/096034012X13316633785757.
[42] Yoo KB, He Y, Lee HS, Bae SY, Kim DS, Shin K. Study of the scale formed on super 304H boiler tube steels after long-term steam oxidation at high temperatures. Mater Char Dec. 2018;146:71–80. https://doi.org/10.1016/j.matchar.2018.09.045.
[43] Fernández AG, Rey A, Lasanta I, Mato S, Brady MP, Pérez FJ. Corrosion of alumina-forming austenitic steel in molten nitrate salts by gravimetric analysis and impedance spectroscopy. Mater Corros Mar. 2014;65(3):267–75. https://doi.org/10.1002/maco.201307422.
[44] Zhou Q, et al. New insight on the formation of uneven oxide scales on AFA steel in supercritical CO2: roles of recrystallization degree on the high temperature corrosion resistance. Corros Sci 2024;241(Dec). https://doi.org/10.1016/j.corsci.2024.112540.
[45] Buscail H, et al. Role of Na2CO3 on an AISI 330 austenitic stainless steels oxidation at 900°C. Mater Corros Aug. 2019;70(8):1416–25. https://doi.org/10.1002/maco.201810567.
[46] Zhang K, et al. Anomalous oxidation behavior and enhanced corrosion resistance of a lean-Cr FeCrAl alloy in the oxygenated PWR primary water. Corros Sci 2026;259(Feb). https://doi.org/10.1016/j.corsci.2025.113452.
[47] American Petroleum Institute. STANDARD, A. P. I. 650, welded steel tanks for oil storage. 2001.
[48] E ASM. Boiler, A. S. M. E., & code, P. V. Section VIII. 2007.
[49] ASTM. Astm G111-97: standard guide for corrosion tests in high temperature or high pressire environment, or both. 2013.
[50] Goods SH, Bradshaw RW. Corrosion of stainless steels and carbon steel by molten mixtures of commercial nitrate salts. J Mater Eng Perform 2004;13(1):78–87. https://doi.org/10.1361/10599490417542.
[51] Elbakhshwan M, Lee DH, Anderson M. Corrosion resistance of high nickel alloys in solar salt at 600 °C for up to 4000 h. Sol Energy Mater Sol Cell 2022;245(Sep). https://doi.org/10.1016/j.solmat.2022.111837.
[52] Prieto C, Ruiz-Cabañas FJ, Madina V, Fernández AI, Cabeza LF. Corrosion performance of alloy 800H and alloy 625 for potential use as molten salts solar receiver materials in concentrating solar power tower plants. J Energy Storage 2022;55(Nov). https://doi.org/10.1016/j.est.2022.105824.

[53] Dorcheh AS, Durham RN, Galetz MC. Corrosion behavior of stainless and low-chromium steels and IN625 in molten nitrate salts at 600 °C. Sol Energy Mater Sol Cell Jan. 2016;144:109–16. https://doi.org/10.1016/j.solmat.2015.08.011.
[54] Wang W, Guan B, Li X, Lu J, Ding J. Corrosion behavior and mechanism of austenitic stainless steels in a new quaternary molten salt for concentrating solar power. Sol Energy Mater Sol Cell 2019;194:36–46.
[55] Kruizenga AM, Gill DD, Laford M. Materials corrosion of high temperature alloys immersed in 600°C binary nitrate salt [Online]. Available: http://www.ntis.gov/help/ordermethods.asp?loc=7-4-0#online; 2013.
[56] Gomes A, Navas M, Uranga N, Paiva T, Figueira I, Diamantino TC. High-temperature corrosion performance of austenitic stainless steels type 316 321. Solar Salt Solar Energy 2019;177:408–19.
[57] Trent MC, Goods SH, Bradshaw RW. Comparison of corrosion performance of grade 316 and grade 347H stainless steels in molten nitrate salt. In: AIP conference proceedings. American Institute of Physics Inc.; May 2016. https://doi.org/10.1063/1.4949258.
[58] Bradshaw RW, Goods SH. Corrosion resistance of stainless steels during thermal cycling in alkali nitrate molten salts. In: Albuquerque, NM, and Livermore, CA (United States); 2001 [Online]. Available: http://www.doe.gov/bridge.
[59] Shi P, et al. Tribological behavior of 316H stainless steel in NaNO3-KNO3 molten salt at elevated temperature. Sol Energy Mater Sol Cell 2023;257(Aug). https://doi.org/10.1016/j.solmat.2023.112377.
[60] Attia AA, Ali A-H, Masri ANA, Baraka AM. Corrosion behaviour of stainless steel alloys in molten (Na,K)NO 3 eutectic mixture. Mater Werkst: Entwicklung, Fertigung, Prüfung, Eigenschaften und Anwendungen technischer Werkstoffe 1999;30:559–65.
[61] Cuevas Arteaga C. Corrosion evaluation of AISI-309 exposed to 50 mol% Na 2 SO 4-50 mol% V 2 O 5 at high temperature applying electrochemical techniques and the weight loss method [Online]. Available: www.electrochemsci.org; 2012.
[62] Biedenkopf P, Spiegel M, Grabke HJ. High temperature corrosion of low and high alloy steels under molten carbonate fuel cell conditions. Mater Corros 1997;48:477.
[63] Wang G, Zhang C, Ma L, Wu Y, Lu Y. Dynamic hot corrosion behavior of austenitic stainless steels in binary nitrate-carbonate molten salts at 600°C. Sol Energy Mater Sol Cell 2025;285(Jun). https://doi.org/10.1016/j.solmat.2025.113533.
[64] Na H, Zhang C, Wu Y, Wang G, Bao G, Lu Y. Thermal stability and corrosion characteristic analysis of low melting point ternary molten salt for thermal energy storage. Sol Energy Mater Sol Cell 2025;286(Jul). https://doi.org/10.1016/j.solmat.2025.113587.
[65] Na H, Zhang C, Wu Y, Wang G, Lu Y. Effect of Na2CO3 content on thermophysical properties, corrosion behaviors of KNO3-NaNO2 molten salt. Energy Dec. 2024;311. https://doi.org/10.1016/j.energy.2024.133378.
[66] Sotelo-Mazón O, et al. Electrochemical study of the corrosion performance of AISI-309 and AISI-310 exposed in NaVO 3 at high temperature [Online]. Available: www.electrochemsci.org; 2015.
[67] Khan MA, Sundarrajan S, Natarajan S. Hot corrosion behaviour of super 304H for marine applications at elevated temperatures. Anti-Corros Methods & Mater 2017;64(5):508–14. https://doi.org/10.1108/ACMM-04-2015-1528.
[68] Xiao J, et al. Corrosion behavior of different alloys in novel chloride molten salts for concentrating solar power plants. Sol Energy Mater Sol Cell 2025;286(Jul). https://doi.org/10.1016/j.solmat.2025.113531.
[69] Mudali UK, Pujar MG. Pitting corrosion of austenitic stainless steels and their weldments. In: Corrosion of austenitic stainless steels. Elsevier; 2002. p. 74–105. https://doi.org/10.1533/9780857094018.106.
[70] Laycock NJ, Newman RC. Temperature dependence of pitting potentials for austenitic stainless steels above their critical pitting temperature. Corros Sci 1998;40:887–902.
[71] Trentin A, Mardoukhi A, Lambai A, Pohjanne P, Huttunen-Saarivirta E. Pitting corrosion of austenitic and duplex stainless steels in dilute acids at elevated temperature: effect of electrolyte chemistry and material microstructure. Corros Sci May 2025;247. https://doi.org/10.1016/j.corsci.2025.112769.
[72] Wang JH, Su CC, Szklarska-Smialowska Z. Effects of Cl-Concentration and temperature on pitting of AISI 304 stainless steel. Corrosion 1988;44(10):732–7.
[73] Manning PE, Duquette DJ. The effect of temperature (25°-289°C) on pit initiation in single phase and duplex 304L stainless steels in 100 ppm C1-solution. Corros Sci 1980;20:597–609.
[74] Dayal RK. Crevice corrosion of stainless steel. In: Corrosion of austenitic stainless steels. Elsevier; 2002. p. 106–16. https://doi.org/10.1533/9780857094018.117.
[75] Rosenfeld IL. In: Corrosion Localized, Staehle RW, Brown BF, Kruger J, Agarwal A, editors. Crevice corrosion of metals and alloys. NACE; 1974. p. 373.
[76] Rosenfeld IL, Marshakov IK. Mechanism of crevice corrosion. Corrosion 1964;20:115–25.
[77] Brigham RJ. Temperature as a crevice corrosion criterion. Corrosion 1974;30:396–8.
[78] Dayal RK, Parvathavarthini N, Gnanamoorthy JB, Rodriguez P, Prasad YVRK. Intergranular attack during crevice corrosion of stainless steels. Mater Lett 1984;2(3):248–52.
[79] Betts AJ, Boulton LH. Crevice corrosion: review of mechanisms, modelling, and mitigation. Br Corrosion J 1993:279–96.
[80] Kaul R, et al. Failure analysis of carbonate reboiler heat exchangers. Eng Fail Anal 1995;2(3):165–74.
[81] Saito N, Sakamoto H, Sugimoto K. Crevice corrosion of austenitic alloys in high-temperature water. Corrosion 1994;54(9):700–12.
[82] Taylor DF. Crevice corrosion of alloy 600 in high temperature aqueous environments. Corrosion 1979;30(12):550–9.
[83] Chen D, Han EH, Wu X. Effects of crevice geometry on corrosion behavior of 304 stainless steel during crevice corrosion in high temperature pure water. Corros Sci Oct. 2016;111:518–30. https://doi.org/10.1016/j.corsci.2016.04.049.
[84] Trasatti SP, Camona E, Mazza F, Sivieri E. Influence of the exposure of AISI 304L stainless steel at moderately high temperature on the susceptibility to crevice corrosion. J Appl Electrochem 1998;28:1333–41.
[85] Butler EP, Burke MG. Chromium depletion and martensite formation at grain boundaries in sensitised austenitic stainless steel. Acta merall 1986;34(3):557–70.
[86] Hall EL, Briant CL. Chromium depletion in the vicinity of carbides in sensitized austenitic stainless steels. Metall Trans A 1984;15:793–811.
[87] Kim HP, Kim DJ. Intergranular corrosion of stainless steel. Corros Sci Technol 2018;17(4):183–92. https://doi.org/10.14773/cst.2018.17.4.183.
[88] Parvathavarthini N. Sensitization and testing for intergranular corrosion. In: Corrosion of austenitic stainless steels. Elsevier; 2002. p. 117–38. https://doi.org/10.1533/9780857094018.139.
[89] Teodoro CA, Wolynec S. Sensitization and tunneling corrosion of austenitic type 347 stainless steel. Corrosion 1998;54(2).
[90] Lima AS, Nascimento AM, Abreu HFG, De Lima-Neto P. Sensitization evaluation of the austenitic stainless steel AISI 304L, 316L, 321 and 347. J Mater Sci 2005;40:139–44.
[91] Swaminathan J, Singh R, Gunjan MK, Mahato B. Sensitization induced stress corrosion failure of AISI 347 stainless steel fractionator furnace tubes. Eng Fail Anal Dec. 2011;18(8):2211–21. https://doi.org/10.1016/j.engfailanal.2011.07.015.
[92] sang Lee H, sung Jung J, soo Kim D, bong Yoo K. Failure analysis on welded joints of 347H austenitic boiler tubes. Eng Fail Anal Nov. 2015;57:413–22. https://doi.org/10.1016/j.engfailanal.2015.08.024.
[93] Shabani Mahalli M, Ahmadi A, Sabouri M. Investigation of intergranular stress corrosion cracking in a failed 347H stainless steel furnace tube. Eng Fail Anal 2022;142(Dec). https://doi.org/10.1016/j.engfailanal.2022.106835.
[94] Bahrami A, Mousavi Anijdan SH, Taheri P, Yazdan Mehr M. Failure of AISI 304H stainless steel elbows in a heat exchanger. Eng Fail Anal Aug. 2018;90:397–403. https://doi.org/10.1016/j.engfailanal.2018.04.006.
[95] Kim Y-S, Lee S-Y, Do J-Y, Ahn S-H, Nam K-W. Mechanical properties and immersion characteristics of sensitinized STS310S, STS316L and STS347H in the range of 480~720°C. J Korea Soc Power Syst Eng Jun. 2016;20(3):43–50. https://doi.org/10.9726/kspse.2016.20.3.043.
[96] Ortner SR, Hippsley CA. High temperature brittle intergranular failure in austenitic stainless steels. Mater Sci Technol Jan. 1992;8(10):883–95. https://doi.org/10.1179/mst.1992.8.10.883.
[97] Zhang J, Di H, Wang X. Flow softening of 253 MA austenitic stainless steel during hot compression at higher strain rates. Mater Sci Eng, A 2016;650:483–91. https://doi.org/10.1016/j.msea.2015.10.084.
[98] Gonzaga AC, Barbosa C, Tavares SSM, Zeemann A, Payaõ JC. Influence of post welding heat treatments on sensitization of AISI 347 stainless steel welded joints. J Mater Res Technol Jan. 2020;9(1):908–21. https://doi.org/10.1016/j.jmrt.2019.11.031.
[99] Kina AY, Souza VM, Tavares SSM, Souza JA, de Abreu HFG. Influence of heat treatments on the intergranular corrosion resistance of the AISI 347 cast and weld metal for high temperature services. J Mater Process Technol Apr. 2008;199(1):391–5. https://doi.org/10.1016/j.jmatprotec.2007.08.011.
[100] Kumar V, Arora H, Pandey PK, Rathore V. Analysis of sensitization of austenitic stainless steel by different welding processes: a review. Int J Appl Eng Res 2015;10:17837–48 [Online]. Available: https://www.researchgate.net/publication/281698788.
[101] Cruz-Hernández VL, García-Hernández R, López-Morelos VH, García-Rentería MA, González-Sánchez J. Intergranular corrosion of AISI 347 stainless steel welds obtained under electromagnetic interaction of low intensity. Mater Lett 2022;312(Apr). https://doi.org/10.1016/j.matlet.2022.131679.
[102] Mittal R, Sidhu BS. Oxidation behaviour of T91-347H welds. J Mater Process Technol 2018;261:266–79.
[103] Kant R, Dupont J. Stress relief cracking susceptibility in high temperature alloys. Weld J 2019;98(2):29s–49s.
[104] Auzoux Q. Effect of pre-strain on creep of three aisi 316 austenitic stainless steels in relation to reheat cracking of weld-affected zones. J Nucl Mater 2010;400(2):127–37.
[105] Yoon KB, Yu JM, Nguyen TS. Stress relaxation cracking in 304H stainless steel weld of a chemical reactor serviced at 560°C. Eng Fail Anal Oct. 2015;56:288–99. https://doi.org/10.1016/j.engfailanal.2015.01.014.
[106] Lee HS, Kim BS, Hong SI. Comparison of stress relaxation cracking susceptibility of austenitic stainless steels. Weld J Sep. 2022;101(9):225–39. https://doi.org/10.29391/2022.101.017.
[107] Beigi M, Khosravifard A, Rabiezadeh A, Sani R. Failure analysis and stress relaxation cracking of 321H stainless steel: experimental and finite element analysis. Eng Fail Anal Dec. 2025;182. https://doi.org/10.1016/j.engfailanal.2025.110001.
[108] Py-Renaudie B. Effect of welding on stress relaxation cracking of the austenitic stainless steel AISI 316L(N). Doctoral dissertation, Université Paris sciences et lettres. 2023 [Online]. Available: https://pastel.hal.science/tel-04058959v1.
[109] Pickle T, Hong Y, Vidal J, Augustine C, Yu Z. Stress relaxation cracking susceptibility evaluation in 347H stainless steel welds. Weld World Mar. 2024;68(3):657–67. https://doi.org/10.1007/s40194-024-01678-9.
[110] Hehemann RE. Stress corrosion cracking of stainless steels. Metall Trans A 1985;16A.
[111] Rhodes PR. Mechanism of chloride stress corrosion cracking of austenitic stainless steels. Corrosion 1969;25(11):462–72.

[112] Louthan Jr MR. Initial stages of stress corrosion cracking in austenitic stainless steels. Corrosion 1965;21:288–94.
[113] Ahlers M, Riecke E. Stress corrosion cracking in single crystals of Fe-25Cr-20Ni. Corros Sci 1978;18:21.
[114] Chen YY, Liou YM, Shih HC. Stress corrosion cracking of type 321 stainless steels in simulated petrochemical process environments containing hydrogen sulfide and chloride. Mater Sci Eng, A Oct. 2005;407(1–2):114–26. https://doi.org/10.1016/j.msea.2005.07.011.
[115] Alekseev AB, Averin SA, Geferova MN, Kondrat'Ev VP, Shikhalev VS. Corrosion resistance of austenitic steels and alloys in high temperatures. J Nucl Mater 1996;233:367–1371.
[116] Shalaby HM, Ravindranath K, Tanoli N, Al-Wakaa B. Failure of 321 stainless steel heater tube in heavy crude oil. Case Stud Eng Fail Anal Oct. 2017;9:1–8. https://doi.org/10.1016/j.csefa.2017.04.004.
[117] Abou-Elazm A, Abdel-Karim R, Elmahallawi I, Rashad R. Correlation between the degree of sensitization and stress corrosion cracking susceptibility of type 304H stainless steel. Corros Sci Feb. 2009;51(2):203–8. https://doi.org/10.1016/j.corsci.2008.10.015.
[118] Messler RW, Li L. Weld heat affected zone liquation cracking in type 347 stainless steel. Sci Technol Weld Join 1997;2(2):43–52 [Online]. Available: http://www.instmat.co.uk.
[119] Shayegani M, Zakersafaee P. Failure analysis of reactor heater tubes SS347H in ISOMAX unit. Eng Fail Anal Jun. 2012;22:121–7. https://doi.org/10.1016/j.engfailanal.2012.01.015.
[120] Fink C, Wang H, Alexandrov BT, Penso J. Filler metal 16-8-2 for structural welds on 304H and 347H stainless steels for high-temperature service. Weld J Dec. 2020;99(12):312s–22s. https://doi.org/10.29391/2020.99.029.
[121] Indig ME, McIlree AR. High temperature electrochemical studies of the stress corrosion of type 304 stainless steel. Corrosion 1979;35(7):288–95.
[122] Silva L de Le, et al. Effects of mechanical stress on the corrosion behaviour of an austenitic stainless steel welded joint – stress corrosion cracking susceptibility. Corros Sci 2025;244(Mar). https://doi.org/10.1016/j.corsci.2024.112629.
[123] Ramirez–Ledesma AL, Acosta–Vargas LA, Juarez–Islas JA. Suppression of interdendritic segregation during welding of a 347 austenitic stainless steel pipe reactors. Eng Fail Anal 2020;114(Aug). https://doi.org/10.1016/j.engfailanal.2020.104589.
[124] Jun YO, Sang Lee B, Chul Kwon S, Hwa Hong J. Ductile fracture mechanisms in shielded metal-arc and gas tungsten-arc welds of type 347 stainless steels. J Mater Sci 1999;34:4751–9.
[125] Zhou Y, et al. A precipitation hardened austenitic stainless steel with excellent stress corrosion cracking resistance against high-temperature water. Corros Sci 2025;257(Dec). https://doi.org/10.1016/j.corsci.2025.113352.
[126] Prabha B, Sundaramoorthy P, Suresh S, Manimozhi S, Ravishankar B. Studies on stress corrosion cracking of super 304h austenitic stainless steel. J Mater Eng Perform Dec. 2009;18(9):1294–9. https://doi.org/10.1007/s11665-008-9347-9.
[127] Sarvghad M, Bell S, Raud R, Steinberg TA, Will G. Stress assisted oxidative failure of inconel 601 for thermal energy storage. Sol Energy Mater Sol Cell Jan. 2017;159:510–7. https://doi.org/10.1016/j.solmat.2016.10.008.
[128] Rumman R, et al. Cracking failure in a 253 MA-Weld-Haynes 230 concentrated solar power receiver. In: Asia-Pacific solar research conference; 2021.
[129] He J, Sandström R. Basic modelling of creep rupture in austenitic stainless steels. Theor Appl Fract Mech Jun. 2017;89:139–46. https://doi.org/10.1016/j.tafmec.2017.02.004.
[130] Needham NG, Gladman T. Nucleation and growth of creep cavities in a type 347 steel. Met Sci Feb. 1980;14(2):64–72. https://doi.org/10.1179/030634580790426300.
[131] Le May I. Failure mechanisms and metallography: a review. Metallography in failure analysis. 1978. p. 1–31.
[132] Cao ZB, Li PE, Zhang JS, Zhu SJ. Creep crack propagation at elevated temperature in a heat-resistant steel. 1988.
[133] Konosu S. Elevated temperature low-cycle fatigue behavior OF HK40 alloy. 1994.
[134] Pilloni G, Quadrini E, Spigarelli S. Interpretation of the role of forest dislocations and precipitates in high-temperature creep in a Nb-stabilised austenitic stainless steel. Mater Sci Eng, A 2000;279:52–60.
[135] Erneman J, Schwind M, Liu P, Nilsson JO, Andrén HO, Ågren J. Precipitation reactions caused by nitrogen uptake during service at high temperatures of a niobium stabilised austenitic stainless steel. Acta Mater Aug. 2004;52(14):4337–50. https://doi.org/10.1016/j.actamat.2004.06.001.
[136] Spindler MW, Knowles G, Jacques S, Austin C. Creep fatigue behaviour of type 321 stainless steel at 650°C. Mater A T High Temp Nov. 2014;31(4):284–304. https://doi.org/10.1179/0960340914Z.00000000051.
[137] Parker JD. High temperature failure of thick-section, low alloy steel to stainless steel transition welds. Mater A T High Temp 1994;12(1):25–33. https://doi.org/10.1080/09603409.1994.11689467.
[138] Anwar MS, Widjaya RR, Prasetya LBA, Arfi AA, Mabruri E, Siradj ES. Effect of grain size on mechanical and creep rupture properties of 253 MA austenitic stainless steel. Metals May 2022;12(5). https://doi.org/10.3390/met12050820.
[139] Shalchi Amirkhiz B, Xu S, Scott C. Microstructural assessment of 310S stainless steel during creep at 800 °C. Materialia 2019;6(Jun). https://doi.org/10.1016/j.mtla.2019.100330.
[140] Pavan AHV, Ravibharath R, Singh K. Creep-rupture behavior of SUS 304h – in 617 dissimilar metal welds for AUSC boiler applications. In: Materials science forum. Trans Tech Publications Ltd; 2015. p. 199–202. https://doi.org/10.4028/www.scientific.net/MSF.830-831.199.
[141] Singh P, Arora N, Sharma A. Enhancing mechanical properties and creep performance of 304H and inconel 617 superalloy dissimilar welds for advanced ultra super critical power plants. Int J Pres Ves Pip Feb. 2023;201. https://doi.org/10.1016/j.ijpvp.2022.104882.
[142] Jiang Y, Kan Y, Chen H. Heterogeneous microstructure-induced creep failure responses in various sub-zones of modified 310S welded joints. Metals Jan. 2022;12(1). https://doi.org/10.3390/met12010116.
[143] O'dowd NP, Nikbin KM, Biglari FR, Wimpory RC, O'donnell MP. Computational and experimental studies of high temperature crack growth in the presence of residual stress [Online]. Available: http://www.asme.org/about-asme/terms-of-use; 2006.
[144] Sakanashi Y, Gungor S, Forsey AN, Bouchard PJ. Measurement of creep deformation across welds in 316H stainless steel using digital image correlation. Exp Mech Feb. 2017;57(2):231–44. https://doi.org/10.1007/s11340-016-0245-z.
[145] Osman H, Nor FM, Hamdan YM, Tamin MN. Creep ruptures of AISI 347 austenitic stainless steel foils at elevated temperature of 750 °C. Proc Inst Mech Eng Part L Sep. 2017;231(6):516–22. https://doi.org/10.1177/1464420715601700.
[146] Shalchi Amirkhiz B, Xu S. Creep properties and tem characterization of 347H stainless steel [Online]. Available: https://www.researchgate.net/publication/308727090; 2016.
[147] Mamun AA, Moat RJ, Kelleher J, Bouchard PJ. Generation of intergranular strains during high temperature creep fatigue loading of 316H stainless steel. Mater A T High Temp Nov. 2014;31(4):378–82. https://doi.org/10.1179/0960340914Z.00000000045.
[148] Calmunger M, Chai G, Johansson S, Moverare J. Creep and fatigue interaction behavior in sanicro 25 heat resistant austenitic stainless steel. Trans Indian Inst Met Mar. 2016;69(2):337–42. https://doi.org/10.1007/s12666-015-0806-3.
[149] González-Rodríguez JG, Luna-Ramírez A, Martínez-Villafañe A. Effect of hot corrosion on the creep properties of types 321 and 347 stainless steels. J Mater Eng Perform 1999;8:91–7.
[150] Purzyńska H, Golański G, Sroka M, Sasiela A, Zieliński A. Microstructure characterization and mechanical properties of austenitic super 304H steel after operation. Int J Pres Ves Pip Oct. 2024;211. https://doi.org/10.1016/j.ijpvp.2024.105294.
[151] Eaton-Mckay J, Yan K, Callaghan MD, Jimenez-Melero E. Creep performance of carburized 316H stainless steel at 550 °C. J Nucl Mater 2022;558(Jan). https://doi.org/10.1016/j.jnucmat.2021.153329.
[152] Helmersson B, Navas M, Martínez-Tarifa A, Wu R, Backhouse A. Molten nitrate corrosion testing and creep data for stainless steels. In: AIP conference proceedings. American Institute of Physics Inc.; Dec. 2020. https://doi.org/10.1063/5.0031284.
[153] Prieto C, Barreneche C, Martínez M, Cabeza LF, Fernández AI. Thermomechanical testing under operating conditions of A516Gr70 used for CSP storage tanks. Sol Energy Mater Sol Cell Jan. 2018;174:509–14. https://doi.org/10.1016/j.solmat.2017.09.029.
[154] Li H, et al. Degradation of 316 L steel under corrosion-creep interaction in solar salt: effects of stress levels and chloride impurities. J Energy Storage Dec. 2025;138. https://doi.org/10.1016/j.est.2025.118492.
[155] Chai G, Forsberg U. Sanicro 25: an advanced high-strength, heat-resistant austenitic stainless steel. An advanced high-strength, heat-resistant austenitic stainless steel. In: Materials for ultra-supercritical and advanced ultra-supercritical power plants. Elsevier Inc.; 2016. p. 391–421. https://doi.org/10.1016/B978-0-08-100552-1.00012-9.
[156] Kloc L, Dymáček P, Sklenička V. High temperature creep of sanicro 25 austenitic steel at low stresses. Mater Sci Eng, A Apr. 2018;722:88–92. https://doi.org/10.1016/j.msea.2018.02.095.
[157] Pandey RK. Failure analysis of styrene reactor tubes. Eng Fail Anal Dec. 2006;13(8):1314–25. https://doi.org/10.1016/j.engfailanal.2005.10.001.
[158] Rozman KA, Detrois M, Liu T, Gao MC, Jablonski PD, Hawk JA. Long-term creep behavior of a CoCrFeNiMn high-entropy alloy. J Mater Eng Perform Sep. 2020;29(9):5822–39. https://doi.org/10.1007/s11665-020-05103-2.
[159] Jang MH, et al. Effect of tungsten addition on high-temperature properties and: microstructure of alumina-forming austenitic heat-resistant steels. Mater Sci Eng, A 2015;647:163–9. https://doi.org/10.1016/j.msea.2015.09.018.
[160] Yamamoto Y, Brady MP, Santella ML, Bei H, Maziasz PJ, Pint BA. Overview of strategies for high-temperature creep and oxidation resistance of alumina-forming austenitic stainless steels. Apr. 2011. https://doi.org/10.1007/s11661-010-0295-2.
[161] Li W, et al. High-temperature creep property and life prediction of aluminized AISI 321 stainless steel after annealing diffusion treatment. Eng Fail Anal 2021;128(Oct). https://doi.org/10.1016/j.engfailanal.2021.105611.
[162] Bressers J, Steen M. Fatigue and microstructure in austenitic high temperature AHoys. 1991.
[163] Kobayashi K, Yamaguchi K, Hayakawa M, Kimura M. High-temperature fatigue properties of austenitic superalloys 718, A286 and 304L. Int J Fatig Oct. 2008;30(10–11):1978–84. https://doi.org/10.1016/j.ijfatigue.2008.01.004.
[164] Ghalambaz M, Abdollahi M, Eslami A, Bahrami A. A case study on failure of AISI 347H stabilized stainless steel pipe in a petrochemical plant. Case Stud Eng Fail Anal Oct. 2017;9:52–62. https://doi.org/10.1016/j.csefa.2017.07.001.
[165] Segersäll M, Deng D. A comparative study between in- and out-of-phase thermomechanical fatigue behaviour of a single-crystal superalloy. Int J Fatig May 2021;146. https://doi.org/10.1016/j.ijfatigue.2021.106162.
[166] Tu Y, Wang J, Wen Z, He P. Thermomechanical fatigue behavior and lifetime prediction of nickel-based single crystal alloys under varying stress conditions. J Alloys Compd Apr. 2025;1023. https://doi.org/10.1016/j.jallcom.2025.180202.
[167] Ramesh M, Leber HJ, Janssens KGF, Diener M, Spolenak R. Thermomechanical and isothermal fatigue behavior of 347 and 316L austenitic stainless tube and

pipe steels. Int J Fatig May 2011;33(5):683–91. https://doi.org/10.1016/j.ijfatigue.2010.11.005.
[168] Pineau A, Antolovich SD. High temperature fatigue: behaviour of three typical classes of structural materials. Mater A T High Temp May 2015;32(3):298–317. https://doi.org/10.1179/0960340914Z.00000000072.
[169] Taira S. Thermal fatigue and its relation to creep rupture and mechanical fatigue. In: High temperature structures and materials. Elsevier; 1964. p. 187–213. https://doi.org/10.1016/b978-0-08-010580-2.50010-4.
[170] Petráš R, Škorík V, Polák J. Thermomechanical fatigue and damage mechanisms in sanicro 25 steel. Mater Sci Eng, A Jan. 2016;650:52–62. https://doi.org/10.1016/j.msea.2015.10.030.
[171] Hwang JH, et al. Tensile and fatigue properties of Super304H welded joint at elevated temperatures. Int J Fatig 2021;143(Feb). https://doi.org/10.1016/j.ijfatigue.2020.105989.
[172] Xu L, et al. Characterizing microstructural evolution and low cycle fatigue behavior of 316H austenitic steel at high-temperatures. J Nucl Mater Apr. 2021;546. https://doi.org/10.1016/j.jnucmat.2020.152758.
[173] Yang J, Li B, Wang K, Zhao L, Xu L, Chen X. Cyclic deformation behavior and damage mechanism of 316H stainless steel under low-cycle fatigue loading at 650 °C. Int J Fatig 2024;188(Nov). https://doi.org/10.1016/j.ijfatigue.2024.108523.
[174] Yamaguchi K, Kanazawa K, Yoshida S. Dependence of temperature and strain rate on the low-cycle fatigue life of type 321 stainless steel. Tetsu-To-Hagane 1978;64(8):1199–208.
[175] Oh Y-J, Hwang T-B, Shin BM. A comparison of low-cycle fatigue properties in stainless steel types 347N and 316N. Mater Trans 2005;46(2):317–22.
[176] Koo GH, Yoon JH. Inelastic material models of type 316H for elevated temperature design of advanced high temperature reactors. Energies Sep. 2020;13(17). https://doi.org/10.3390/en13174548.
[177] Pardal JM, Carvalho SS, Barbosa C, Montenegro TR, Tavares SSM. Failure analysis of AISI 310S plate in an inert gas generator used in off-shore oil platform. Eng Fail Anal Sep. 2011;18(6):1435–44. https://doi.org/10.1016/j.engfailanal.2011.04.005.
[178] Tang Z, et al. A review study for physical characteristics and engineering perspectives of dual molten salt tanks. Elsevier Ltd; 2026. https://doi.org/10.1016/j.applthermaleng.2025.128840.
[179] González-Gómez PA, Rodríguez-Sánchez MR, Laporte-Azcué M, Santana D. Calculating molten-salt central-receiver lifetime under creep-fatigue damage. Sol Energy Jan. 2021;213:180–97. https://doi.org/10.1016/j.solener.2020.11.033.
[180] Zhan J, Li M, Huang J, Bi H, Li Q, Gu H. Thermal fatigue characteristics of type 309 austenitic stainless steel for automotive manifolds. Metals Feb. 2019;9(2). https://doi.org/10.3390/met9020129.
[181] J. .-0 Nilsson. The influence of nitrogen on high temperature low cycle fatigue behaviour of austenitic stainless steels. 1984.
[182] Sandstrom R, Engstrom J, Nilsson JO, Nordgren A. Elevated temperature low-cycle fatigue of the austenitic stainless steels type 316 and 253MA. Influence of microstructure and damage mechanisms. High Temp Technol 1989;7(1):2–10. https://doi.org/10.1080/02619180.1989.11753406.
[183] Bochnowski W, Szyller Ł, Osetek M. Damage characterization of belt conveyor made of the 330Nb alloy after service in a carburizing atmosphere in a continuous heat treatment furnace. Eng Fail Anal Sep. 2019;103:173–83. https://doi.org/10.1016/j.engfailanal.2019.04.058.
[184] Kim YJ, Lee DG, Jeong HK, Lee YT, Jang H. High temperature mechanical properties of HK40-type heat-resistant cast austenitic stainless steels. J Mater Eng Perform Jul. 2010;19(5):700–4. https://doi.org/10.1007/s11665-009-9550-3.
[185] Liu Z, Tin S. The stress-controlled low cycle fatigue properties of HK40 and HP40 heat-resistant Fe–Ni base alloys. Metall Mater Trans A Phys Metall Mater Sci Nov. 2023;54(11):4545–57. https://doi.org/10.1007/s11661-023-07188-5.
[186] Xing L, Zhao J, zhong Shen F, Feng W. Reliability analysis and life prediction of HK40 steel during high-temperature exposure. Int J Pres Ves Pip Oct. 2006;83(10):730–5. https://doi.org/10.1016/j.ijpvp.2006.07.006.
[187] Santacreu P, Saedlou S, Faivre L, Acher A, Leseux J. Ferritic stainless steel grade with improved durability for high temperature exhaust manifold. In: SAE 2011 World Congress and exhibition; 2011. https://doi.org/10.4271/2011-01-0194.
[188] Gong Q, Hanke A, Kessel F, Bonk A, Bauer T, Ding W. Molten chloride salt technology for next-generation CSP plants: selection of cold tank structural material utilizing corrosion control at 500 °C. Sol Energy Mater Sol Cell May 2023;253. https://doi.org/10.1016/j.solmat.2023.112233.
[189] Zhou Y, et al. Oxide stress and fracture susceptibility on a surface gradient microstructure of an additively manufactured steel. Acta Mater 2026;304(Jan). https://doi.org/10.1016/j.actamat.2025.121779.
[190] Tang Z, Wu Y, Yang Z, Bai F, Cao Y, Tao WQ. Performance analysis of feedback-controlled preheating process for molten salt storage tanks. Appl Therm Eng 2026;284(Jan). https://doi.org/10.1016/j.applthermaleng.2025.129103.
[191] Betancor-Cazorla L, Svobodova-Sedlackova A, Clavé G, Barreneche C, Dosta S. Protective thermal spray coatings for TES applications in CSP plants. Surf Coat Technol 2025;512(Sep). https://doi.org/10.1016/j.surfcoat.2025.132366.
[192] Fu D, Zhang C, Wang G, Na H, Wu Y. An update review of molecular dynamic study on thermal physical properties of molten salt. Sol Energy Mater Sol Cell 2024;273(Aug). https://doi.org/10.1016/j.solmat.2024.112916.

Sergio Andrés Ardila Parra: DIOPMA research group, Departament de Ciència de Materials i Química Física, Universitat de Barcelona, C/ Martí i Franquès 1, 08028, Barcelona, Spain https://scholar.google.es/citations?user=GOkWaMcAAAAJ&hl=es&oi=ao

Cristina Prieto: Department of Energy Engineering, Universidad de Sevilla, 41,092 Sevilla, Spain https://scholar.google.es/citations?user=7mbg8kAAAAAJ&hl=es&oi=ao

Julian D. Osorio: Building Technologies and Science Center, National Renewable Energy Laboratory, Golden, CO 80401, United States of America. https://scholar.google.es/citations?user=41YFTF8AAAAJ&hl=es&oi=ao

Corresponding author: Ana Inés Fernández: DIOPMA research group, Departament de Ciència de Materials i Química Física, Universitat de Barcelona, C/ Martí i Franquès 1, 08028, Barcelona, Spain, ana_inesfernandez@ub.edu. https://scholar.google.es/citations?user=VegeZIgAAAAJ&hl=es&oi=sra